Corrosion Science 233 (2024) 112092

Contents lists available at ScienceDirect

Corrosion Science

journal homepage: www.elsevier.com/locate/corsci

Local crack arrestability and deformation microstructure evolution of hydrogen-related fracture in martensitic steel

Akinobu Shibata [a,b,*], Ivan Gutierrez-Urrutia [a], Akiko Nakamura [c], Taku Moronaga [c], Kazuho Okada [a], Yazid Madi [d], Jacques Besson [d], Toru Hara [a]

[a] *Research Center for Structural Materials, National Institute for Materials Science (NIMS), 1-2-1, Sengen, Tsukuba 305-0047, Japan*
[b] *PRESTO, Japan Science and Technology Agency, 4-1-8 Honcho, Kawaguchi, Saitama 332-0012, Japan*
[c] *Research Network and Facility Services Division, National Institute for Materials Science (NIMS), 1-2-1, Sengen, Tsukuba 305-0047, Japan*
[d] *Centre des Matériaux, MINES Paris-PSL, CNRS UMR 7633, BP 87, Evry 91003, France*

ARTICLE INFO

Keywords:
Steel (A)
SEM (B)
STEM (B)
Hydrogen embrittlement (C)

ABSTRACT

Intergranular cracks in the uncharged specimen were arrested at low-angle prior austenite grain boundary (PAGB) segments of several micrometers. In contrast, even small, low-angle PAGB segments with sub-micrometer sizes impeded the propagation of hydrogen-related intergranular crack. At the hydrogen-related quasi-cleavage crack tip, the crystallographic orientation changed abruptly, and deformation microstructures developed, including the formation of low-energy dislocation structures. A certain degree of crack growth resistance (intrinsic crack growth resistance) in the hydrogen-related fractures could be attributed to the intense localized plastic works involved in the arrest of intergranular cracks and the propagation of quasi-cleavage cracks.

1. Introduction

To reduce greenhouse gas emissions and achieve a carbon-neutral society, the transportation sector must focus on reducing the weight of vehicle bodies and improving fuel efficiency by applying high-strength steels to various parts of vehicles. Therefore, advanced high-strength steels are being developed worldwide to improve fuel economy. However, hydrogen embrittlement hinders the widespread application of high-strength steels. Hydrogen embrittlement is a phenomenon in which hydrogen is absorbed by materials, making them brittle and prone to sudden failure. Research on hydrogen embrittlement has traditionally focused on materials used in harsh hydrogen environments. However, as the material strength increases (tensile strength becomes higher than 1.2 GPa), the risk of hydrogen embrittlement increases even in natural atmospheric environments. Therefore, it is necessary to improve the hydrogen embrittlement properties of high-strength steels to enable their widespread use in commercial products, such as vehicle bodies.

Several hydrogen-related fracture models have been proposed, including the hydrogen-enhanced decohesion (HEDE) [1–3], hydrogen-enhanced localized plasticity (HELP) [4–8], hydrogen-enhanced strain-induced vacancy (HESIV) [9–11], etc. The HEDE model assumes that the presence of hydrogen reduces the atomistic cohesive energy at the grain boundaries and/or specific crystallographic planes, leading to brittle fracture. The HELP model proposes that hydrogen increases the dislocation mobility and localizes shear deformation in the crack tip region, thereby facilitating the progression of ductile fracture. The HESIV model considers that hydrogen facilitates the formation of vacancies and their coalescence during plastic deformation, promoting ductile fracture. There has been much debate within the scientific community regarding the validity of these proposed models. Recent research suggests that hydrogen embrittlement is the result of a combination of these fracture models, and the predominant model in hydrogen-related fractures is influenced by several factors such as the material strength level, microstructure, deformation conditions (temperature, strain rate, etc.), and hydrogen content. However, the relationship between the macroscopic mechanical response and each fracture model remains unclear.

Martensitic steel is a typical high-strength steel. The martensite structure consists of several structural units with different sizes, that is, laths, blocks, packets, and prior austenite grains (PAGs) [12–17]. A lath is the smallest structural unit and has a high dislocation density ($\rho = \sim 10^{15}\ \mathrm{m}^{-2}$ [18]). A block is an aggregation of laths with nearly identical crystallographic orientations, whereas a packet comprises several blocks with almost identical habit plane orientations. A PAG corresponds to the

---

* Corresponding author at: Research Center for Structural Materials, National Institute for Materials Science (NIMS), 1-2-1, Sengen, Tsukuba 305-0047, Japan.
E-mail address: SHIBATA.Akinobu@nims.go.jp (A. Shibata).

https://doi.org/10.1016/j.corsci.2024.112092
Received 19 March 2024; Received in revised form 16 April 2024; Accepted 24 April 2024

original grain in the parent austenite phase before martensitic transformation. Although several types of high-angle boundaries exist in the martensite structure, namely block boundaries, packet boundaries, and prior austenite grain boundaries (PAGBs), hydrogen-related intergranular fractures mainly occur at PAGBs [19–26]. Through martensitic transformation, several martensite variants nucleate and stop growing at the original austenite grain boundaries [27–29]. Consequently, each austenite grain boundary is subdivided into several separate segments, which share a common spatial boundary plane but possesses different crystallographic characteristics [30]. That is, PAGBs exhibit an uneven structure from a crystallographic perspective. Although the basic mechanism of hydrogen-related intergranular fracture is straightforward and is caused by hydrogen-induced reduction of cohesive energy of PAGBs, the crack propagation behavior is intricate because of the heterogeneous structure of the PAGBs. Quasi-cleavage fracture, another typical hydrogen-related fracture mode, corresponds to a transgranular fracture inside the PAGs. The resultant fracture surface consists of serrated markings (or referred to as tear ridges) that differ from the river patterns on the cleavage plane. Several studies have proposed that quasi-cleavage fractures occur at lath boundaries [31–34]. However, it is difficult to explain the reason for the preferential occurrence of decohesion at lath boundaries instead of block boundaries, packet boundaries, and PAGBs, because lath boundaries are low-angle boundaries whose misorientation angle is usually less than 3 ° [15]. Recent research has provided clear evidence that quasi-cleavage cracks propagate inside the lath rather than at the lath boundaries [35,36]. Additionally, the crystallographic planes associated with quasi-cleavage fracture remain controversial. Some studies have suggested that quasi-cleavage fractures occur along the {0 1 1} planes [11,23,31,32,35–40], whereas others have reported that the quasi-cleavage fracture plane corresponds to the {0 0 1} planes [34,41,42], which are the same as the cleavage plane in body-centered cubic (bcc) crystals. It has been considered that local plastic deformation plays a crucial role in quasi-cleavage fractures [11,36,43]. However, the detailed plastic deformation behavior that accompanies quasi-cleavage fractures is not yet understood.

To quantitatively understand the origin of the macroscopic mechanical response associated with hydrogen embrittlement (such as fracture toughness, crack-growth resistance, and so on), the crack propagation and local plastic deformation behaviors should be precisely characterized. The combination of focused ion beam-scanning electron microscopy (FIB-SEM) serial sectioning and electron backscattering diffraction (EBSD) allows for three-dimensional (3D) microstructural / crystallographic characterization at the microscopic scale [44–46]. In particular, the factors that control local crack arrestability can be effectively studied using the 3D-EBSD technique [30,47]. Recently, conventional two-dimensional (2D) EBSD analysis has been used to study the plastic deformation behavior associated with hydrogen-related crack propagation [48–50]. Although detailed studies on deformation microstructure characterization using transmission electron microscopy (TEM) have been limited, it is necessary to understand the local plastic deformation associated with hydrogen-related crack propagation. Previously, we applied 3D characterization technique to investigate intergranular fracture behavior in as-quenched martensitic steel and revealed that the character of each segment of PAGB affected crack propagation behaviors [30,47]. This study advances the understanding of local crack arrestability and plastic deformation behaviors of hydrogen-related fractures by employing more detailed 3D characterization and advanced TEM techniques. Furthermore, it provides comprehensive discussions on the underlying mechanism of hydrogen-related fracture and origin of the mechanical response associated with hydrogen embrittlement.

2. Material and methods

The material used in the present study is an Fe-8Ni-0.1 C alloy. The detailed chemical composition is C: 0.116, Si: 0.005, Mn: 0.01, P: 0.001, S:0.0015, Al: 0.033, Ni: 7.94, and Fe: balance (mass%). The as-received plates were austenitized at 1000 °C for 30 min, followed by ice-brine quenching and sub-zero cooling in liquid nitrogen to obtain a fully martensitic microstructure. We confirmed that there were no pro-eutectoid ferrite and retained austenite in the heat-treated specimens. From the heat-treated plates, compact tension specimens were prepared. The dimensions of the specimen were width: 25 mm and thickness: 12.5 mm. The pre-crack was introduced through fatigue deformation with a load ratio of 0.1. Initially, the stress intensity factor was 20 MPa $m^{1/2}$, then successively decreased to 12 MPa $m^{1/2}$ by the end. The initial crack length including fatigue pre-crack was 11.25 ~ 13.75 mm ($a_0/W =$ 0.45 ~ 0.55). After the pre-cracking, side grooves were introduced to achieve a net thickness of 10 mm at the root of the side grooves. Hydrogen was introduced into the pre-cracked specimen via electrochemical charging in an aqueous solution containing 3% NaCl and 3 g L^{-1} NH_4SCN for 3 days at ambient temperature. From our preliminary experiments, we confirmed that a charging period of 3 days adequately achieved a uniform distribution of hydrogen in the geometry of the used specimen. The current densities employed for hydrogen charging were 1.25 and 3 A m^{-2}, and the diffusible hydrogen contents measured using thermal desorption analysis were 0.42 and 4.00 wt ppm, respectively. The corresponding thermal desorption curves can be found in [51].

Unloading compliance tests at displacement intervals of 0.025 mm were conducted in air. The J-integral was obtained using $J_{el} + J_{pl}$. J_{el} was calculated by linear elastic fracture mechanics, and J_{pl} was incrementally evaluated from the plastic deformation area under the load – load-line displacement curve. Each unload-reload sequence in test was repeated three times, and the crack extension length (Δa) during the test was calculated using the elastic compliance method outlined in ASTM E1820–17 [52]. To achieve a sufficiently slow strain rate, the load-line displacement was set to 2.5 × 10^{-5} mm s^{-1}, and the corresponding initial rate of the stress intensity factor for $a_0/W = 0.5$ was 8.5 × 10^{-3} MPa $m^{1/2}$ s^{-1}.

Serial sectioning was performed using a xenon-plasma type FIB-SEM system (ThermoFisher Scientific, Helios 5) and an orthogonal gallium ion (Ga^+) beam type FIB-SEM system (Hitachi High-Tech, SMF-1000). A pillar with dimensions of approximately 100 µm × 100 µm × 100 µm (for the xenon-plasma type FIB-SEM system) and 25 µm × 25 µm × 25 µm (for the Ga^+ beam type FIB-SEM system) containing cracks were lifted out from the tested-specimen using an FIB (ThermoFisher Scientific, Helios 5 and Scios 2), and the microscopic 3D crack morphology was analyzed by serial sectioning using the FIB-SEM systems. The pillars were milled at intervals of 10, 50, 100, and 200 nm depending on the analysis volume. The acceleration voltage was 30 kV, and the beam current was 0.7 ~ 13 nA (Ga^+ beam type FIB-SEM system) and 60 nA (xenon-plasma type FIB-SEM system). The microstructural observations and EBSD measurements were performed for each milled surface. A milling interval of 10 nm and 100 nm was employed for the microstructural observations using SEM (acceleration voltage: 2 kV and 5 kV). The step sizes for the EBSD measurements were 50, 100, and 200 nm, which were set to be equal to the milling interval (acceleration voltage: 15 kV and 20 kV). The images acquired by the FIB-SEM serial sectioning were processed using ORS Dragonfly Pro software. DREAM.3D (open-source software) [53] was used to reconstruct the 3D-EBSD orientation maps. The specimen coordinate system was basically configured as follows: $\pm X$ represents the direction parallel to the load-line displacement (that is, macroscopic tensile axis), -Y represents the macroscopic crack propagation direction, and -Z represents the depth direction in the FIB-SEM serial sectioning (the section of $Z = 0$ corresponds to the first observation section). The following results are presented based on this coordinate system.

To fabricate thin foils containing cracks, the cracked areas were preserved using electron and ion beam depositions, and the lifted-out specimens were then thinned using the Ga^+ beam type FIB-SEM system. The substructures of the thin foils were observed using scanning transmission electron microscopy (STEM; JEOL, JEM-2800 and JEM-ARM300F). Local crystal orientation mapping of the thin foils was performed using the STEM-Diffraction technique (automated crystallographic orientation mapping in TEM (ACOM-TEM), NanoMEGAS, ASTAR) with a step size of 2 nm (analyzing area: 3.2 μm × 3.2 μm) and 5 nm (analyzing area: 8 μm × 8 μm). To observe a clear dislocation structure, we employed the two-beam condition with the diffraction vector of $\boldsymbol{g}^* = 0\ 1\ 1$. The dislocation density was measured from the images taken by exciting the diffraction vector of $\boldsymbol{g}^* = 0\,0\,2$, which made all perfect dislocations in bcc crystal visible. The foil thickness of the observed area was determined using electron energy loss spectrometry.

3. Results

3.1. Microstructure and mechanical properties

Fig. 1 presents (a) SEM image, (b – d) STEM images, and (e – g) energy-dispersive X-ray (EDX) analysis results of the as heat-treated specimen ((d) and (g) were reused from our previous study [54]). The specimen exhibits a typical lath martensite structure without any pro-eutectoid ferrite and retained austenite, as shown in Fig. 1(a, b). Although the specimen was in the as-quenched state, the formation of cementite inside lath was confirmed by the electron diffraction pattern and its key diagram (Fig. 1(c)). The cementite holds the Bagaryatskii relationship with the martensite matrix ($[1\,0\,0]_\theta$ // $[1\,1\,1]_M$, $[0\,1\,0]_\theta$ // $[-1-1\ 2]_M$, $[0\ 0\ 1]_\theta$ // $[1-1\ 0]_M$ (the subscripts θ and M indicate cementite and martensite, respectively)). We have confirmed that the presence of cementite did not influence the hydrogen-related crack propagation behavior due to its small fraction. According to the STEM-EDX analysis results, carbon and sulfur, but not nickel, are segregated in the PAGB. The quantitative analysis indicates that the concentration of segregated carbon is 3.58% (nominal concentration = 0.116%) and that of sulfur is 0.12% (nominal concentration = 0.0015%). Bika et al. reported that the dissolution of sulfides during austenitization resulted in the segregation of sulfur in the austenite grain boundaries [55]. Although segregated carbon increases the boundary cohesive energy in steels [56], the occurrence of intergranular fracture even in the uncharged specimen shown in the following can be attributed to the sulfur segregated in the PAGBs.

According to the previously reported uniaxial tensile test results [57], the 0.2% proof strength and tensile strength were 920 and 1191 MPa, respectively. Fig. 2(a - c) presents the $J - \Delta a$ resistance curves, fracture initiation toughness (J_{IC} and K_Q), and dimensionless tearing modulus (T_R) with different H_D obtained from the unloading compliance tests (the data from our previous study [57] was reused). All specimens satisfied the specimen size criteria for obtaining a valid plane-strain J_{IC} according to ASTM E1820–17 [52]. However, the requirements for a valid K_{IC} (ASTM E399–09 [58]) were not satisfied; therefore K_Q is an apparent fracture toughness. The resulting fracture surfaces in the uncharged and hydrogen-charged specimens mainly consisted of intergranular surfaces. Fig. 2(d - f) presents representative SEM images of the fracture surfaces (the uncharged specimen and the hydrogen-charged specimens with H_D = 0.42 and 4.00 wt ppm). The fracture initiation toughness (both J_{IC} and K_Q) decreased significantly with increasing H_D up to 0.5 wt ppm. However, the fracture initiation toughness remained unchanged with a further increase in H_D. This indicates that the small amount of hydrogen at approximately $H_D = 0.5$ wt ppm was sufficient to meet the lower limit of resistance for the onset of crack propagation. Additionally, a positive value of tearing modulus (that is, a certain degree of crack-growth resistance) was confirmed for the hydrogen-related intergranular fracture, even when the H_D was as high as 4.00 wt ppm. This could be attributed to the intrinsic crack growth resistance at microscopic scale.

3.2. Crack propagation behavior

Fig. 3 depicts the microscopic crack propagation behavior in the uncharged specimen analyzed using 3D-EBSD; (a) a SEM image of the first section and (b, c) 3D-EBSD orientation maps (the observation direction of (c) is indicated in (b)). The positions of the PAGBs ahead of the crack are indicated by the white-dashed lines (in the following images,

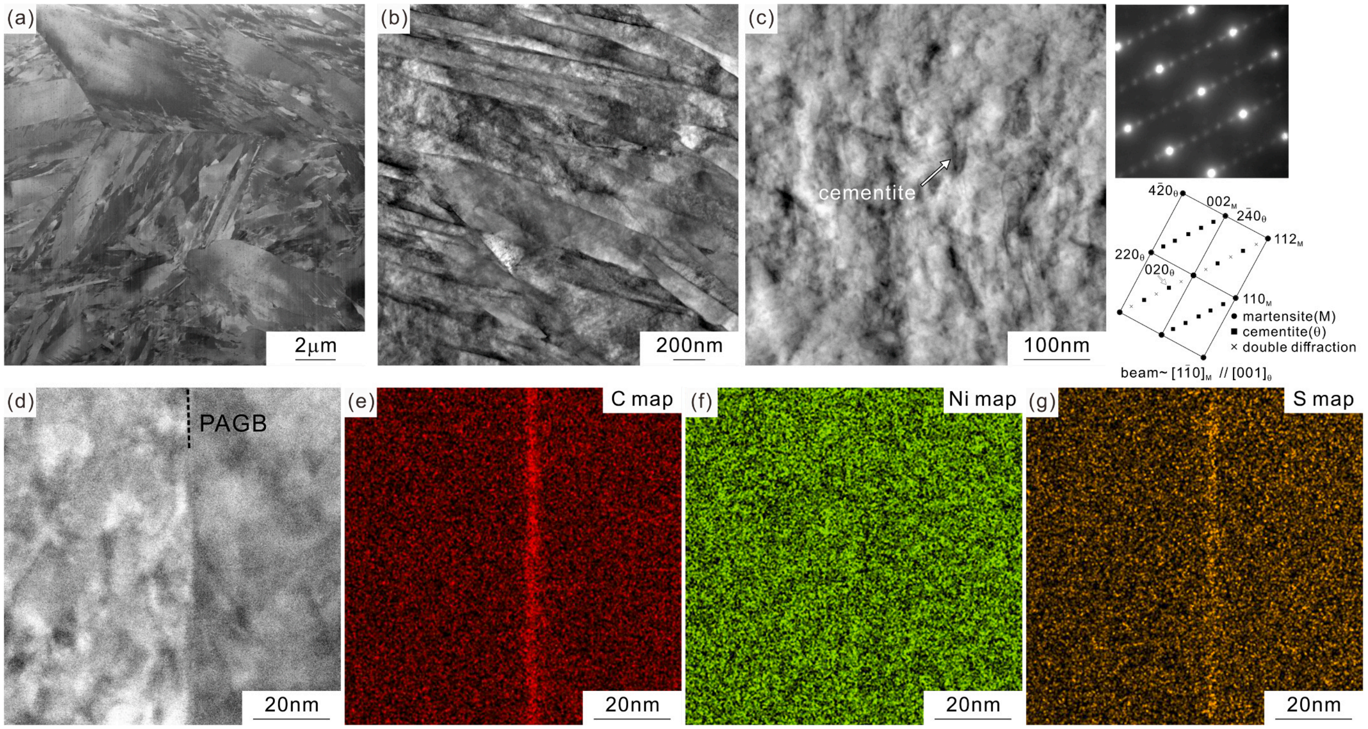

Fig. 1. (a) SEM image, (b - d) STEM images, and (e - g) STEM-EDX analysis results (the distribution maps of (e) carbon, (f) nickel, and (g) sulfur) of the heat-treated specimen. The corresponding electron diffraction pattern and key diagram are also shown in (c).

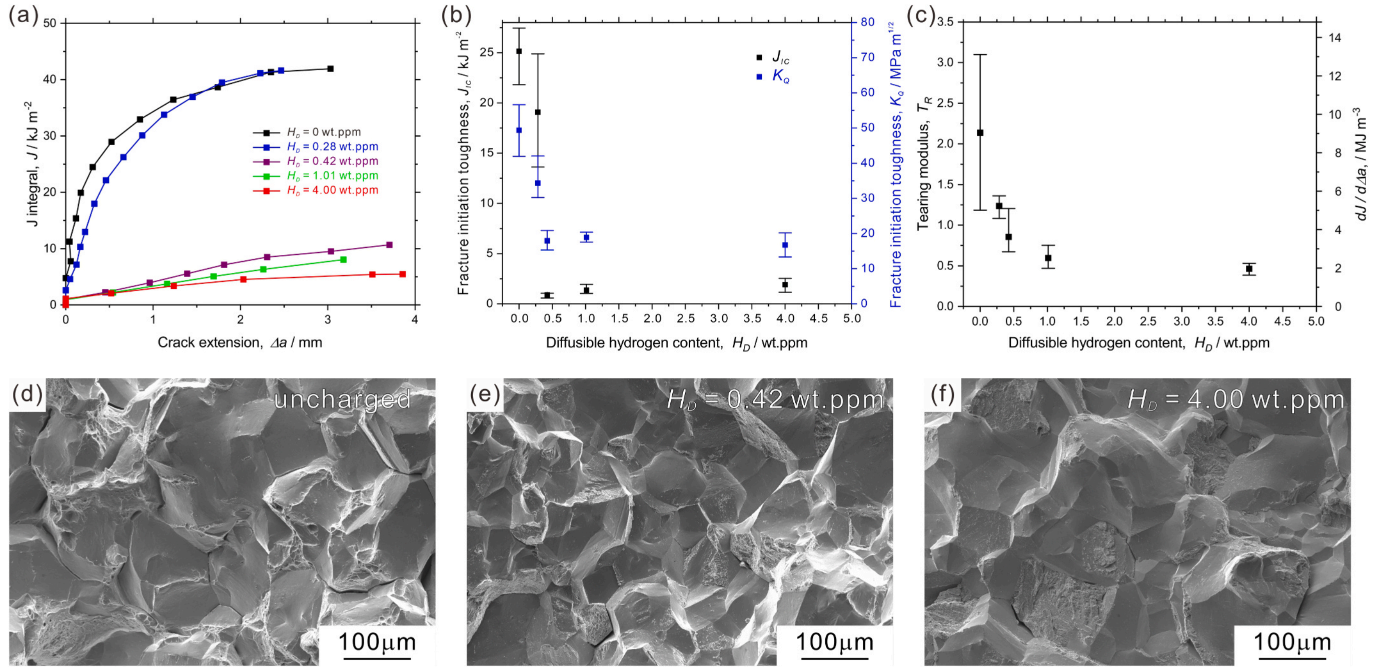

Fig. 2. (a) $J - \Delta a$ resistance curves, (b) fracture initiation toughness (J_{IC} (black) and K_Q (blue)), and (c) tearing modulus with different H_D (the data from our previous paper [57] were reused). (d – f) SEM images of the fracture surfaces of the uncharged specimen (d), hydrogen-charged specimen with $H_D = 0.42$ wt ppm (e), and hydrogen-charged specimen with $H_D = 4.00$ wt ppm (f).

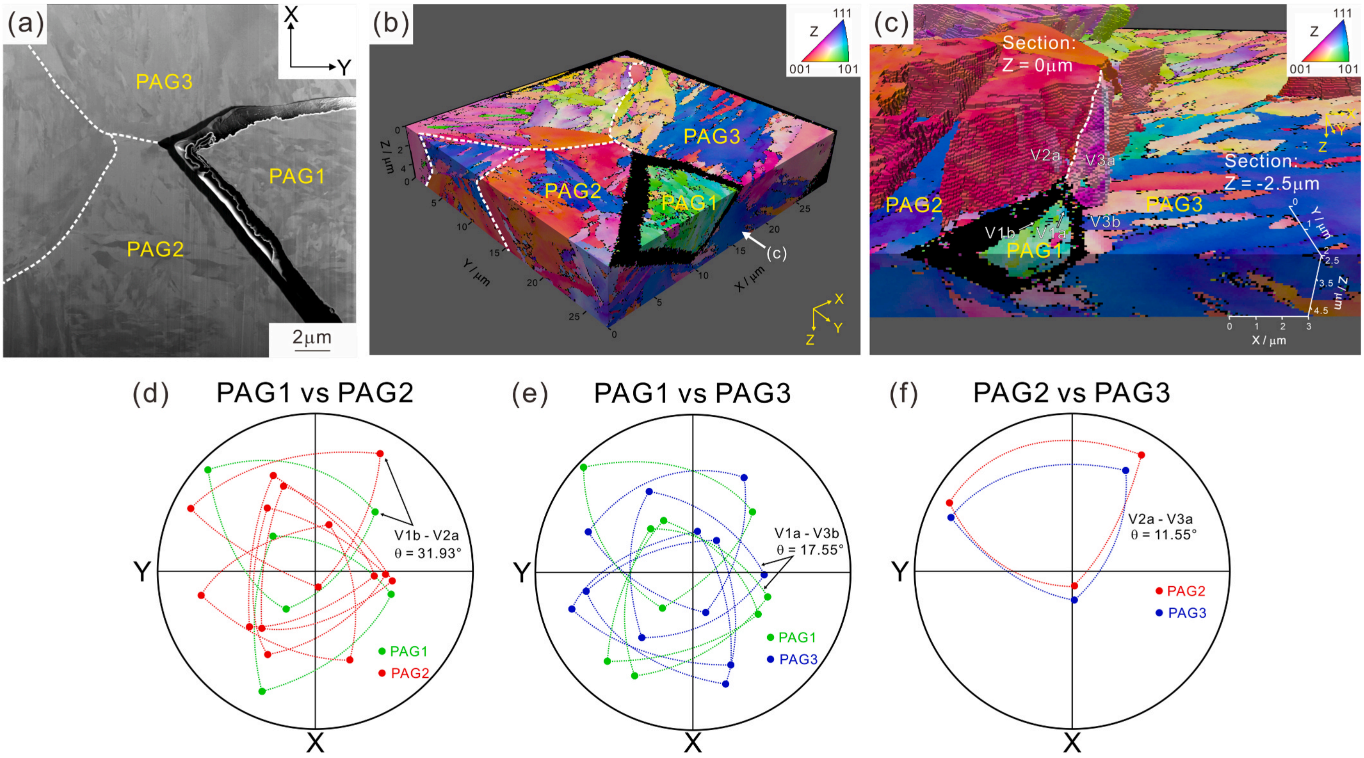

Fig. 3. (a) SEM image ($Z = 0$ μm), (b, c) 3D-EBSD orientation maps of the entire analyzed volume and at the top section $Z = -2.5$ μm, and (d – f) <0 0 1> pole figures showing the orientations of the martensite variants facing the prior austenite grain boundaries.

the white-dashed lines indicate the positions of the PAGBs). The colors in the EBSD orientation maps represent the crystal orientation parallel to the *Z* direction according to the inserted stereographic triangle. The crack propagated at the boundaries between PAG1 and PAG2 and between PAG1 and PAG 3 but was arrested at the boundary between PAG2 and PAG3. Fig. 3(d – f) illustrates the <0 0 1> pole figures of the martensite variants facing the PAGBs. Several martensite variants are observed to be adjacent to the PAG1 / PAG2 and PAG1 / PAG3 boundaries, indicating that the length of each segment at these PAGBs is short (sub-micrometer size). Additionally, Fig. 3(d, e) indicates that the minimum misorientation across the PAGBs is relatively large (31.93 ° between V1b and V2a at the PAG1 / PAG2 boundary and 17.55 ° between V1a and V3b at the PAG1 / PAG3 boundary). In contrast, as shown in Fig. 3(c, f), a large part of the PAG2 / PAG3 boundary (size of several micrometers) consists of a boundary segment between V2a and V3a, whose misorientation is 11.55 ° (the V2a and V3a regions above the observed section ($Z = -2.5$ μm) are displayed in Fig. 3(c)). Accordingly, the results demonstrated that a low-angle PAGB segment of several micrometers in size can act as an obstacle to intergranular crack propagation in the uncharged specimen.

Fig. 4(a, b) shows a SEM image and the corresponding EBSD orientation map of the first section of the hydrogen-charged specimen with $H_D = 0.42$ wt ppm. Cracks propagated at the PAGBs. However, as indicated by the white arrows in Fig. 4(a), numerous very fine uncracked ligaments were formed, and the cracks frequently deviated from the PAGBs, leading to discontinuous crack propagation. The reconstructed 3D morphology of the crack and the corresponding 3D-EBSD orientation map are presented in Fig. 4(c, d), respectively. The frequent deviation of the crack from the PAGB plane can be confirmed in Fig. 4(c) (blue: intergranular crack component, red: quasi-cleavage crack component). Fig. 4(e, f) shows the misorientation profiles of the PAGB segments in the regions indicated in (c), and the misorientation

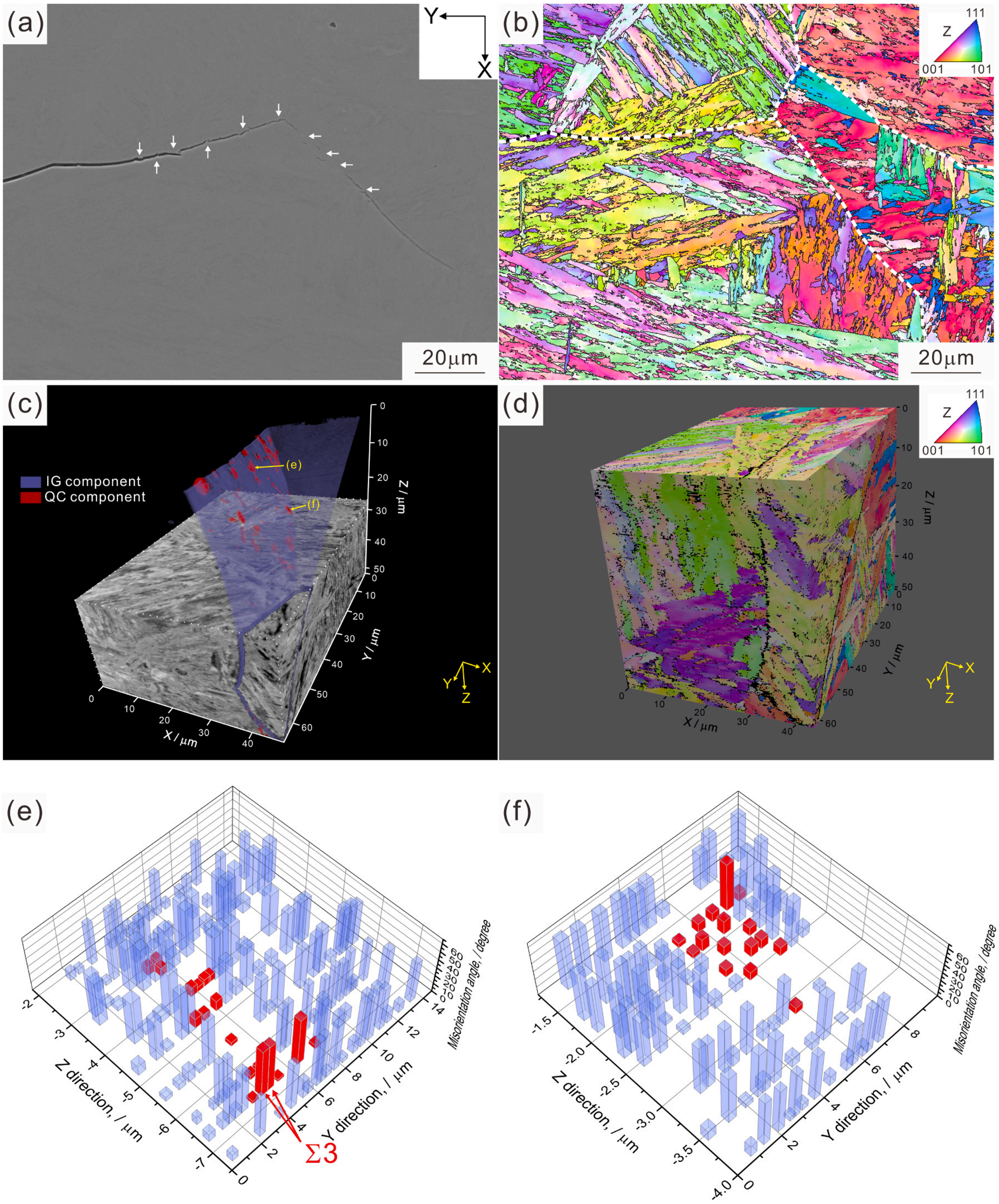

Fig. 4. (a, b) SEM image and EBSD orientation map ($Z = 0$ μm), (c) 3D crack morphology (blue: intergranular crack component and red: quasi-cleavage crack component), (d) 3D-EBSD orientation map, and (e, f) misorientation of the prior austenite grain boundary segments at the regions indicated in (c) of the hydrogen-charged specimen with $H_D = 0.42$ wt ppm.

angle is represented by the height of the bar. The red bars correspond to the positions of the un-cracked ligament, that is, the positions where the intergranular crack was not continuous on the PAGB plane. Although some PAGB segments with large misorientation are involved, the un-cracked ligaments form at the PAGB segments with small misorientations or segments with Σ3 relationship. Therefore, the results shown in Fig. 4 indicate that, in the case of hydrogen-related fractures, low-angle PAGB segments with small size can impede crack propagation.

The results of the 3D-EBSD analysis of the hydrogen-charged specimen with $H_D = 4.00$ wt ppm are shown in Fig. 5 ((a) SEM image of the first section and (b) 3D-EBSD kernel average misorientation (KAM) map). KAM represents the average misorientation around a measurement point. In the present study, orientation data of the three-dimensional neighboring points surrounding a measurement point (26 points in total) were used. Higher KAM values are indicative of significant crystal rotation resulting from plastic deformation. The crack deviated from the PAGB and propagated in a quasi-cleavage manner. The crystallographic plane of the quasi-cleavage component was identified using two-surface trace analysis, and the plane normal was determined to be {0.119 0.652 0.747}, as shown in the stereographic triangle of Fig. 5(c). Although the quasi-cleavage crack plane is close to the {0 1 1} plane, the misorientation from the {0 1 1} plane is 7.76 °. Moreover, the KAM values around the quasi-cleavage crack are remarkably high, indicating crystal rotation owing to plastic deformation (Fig. 5(b)). Because the crack plane does not coincide exactly with the {0 1 1} plane, we can infer that the quasi-cleavage fracture is not due to atomistic cleavage fracture at the {0 1 1} plane but to fracture macroscopically parallel to the {0 1 1} plane, which is accompanied by large plastic deformation. As shown in the <0 1 1> pole figure of Fig. 5 (d), it should be emphasized that the {0 1 1} plane selected as the quasi-cleavage fracture is different from the {0 1 1} plane parallel to the lath and block boundaries. Therefore, we can conclude that the quasi-cleavage fracture does not originate from the decohesion at the lath / block boundaries.

Fig. 6 presents the 3D-EBSD analysis result in the hydrogen-charged specimen with $H_D = 4.00$ wt ppm. As shown in the low- (Fig. 6(a)) and high-magnification (Fig. 6(b)) SEM images and the EBSD orientation map (Fig. 6(c)) of the first section, an ultrafine-grained structure with a grain size less than 1 μm formed around the intergranular crack. Fig. 6 (d) illustrates the <0 0 1> pole figure of the white rectangular area in (c) (the colors in the poles correspond to that in the EBSD orientation map). The orientation of parent austenite phase on the left side before the transformation was recalculated from the EBSD orientation data assuming the Kurdjumov-Sachs (K-S) orientation relationship between martensite and austenite [59]. The ideal <0 0 1> poles of the 24 K-S variants are indicated by black circles. Because the distribution of the <0 0 1> poles is different from that of the ideal 24 K-S variants, we can say that grain subdivision due to severe plastic deformation occurred around the intergranular crack. Fig. 6(e – h) presents the 3D-EBSD orientation maps and 3D-EBSD KAM maps, respectively, with arbitrary sections. The crack exhibits a large opening displacement below the ultrafine-grained region, and the KAM values are particularly high in the ultrafine-grained region. This indicates that plastic deformation sufficiently large to form an ultrafine-grained structure occurred locally at the crack tip with a large opening displacement. Although only one example is shown in this paper (Fig. 6), we have observed several arrested intergranular crack tips where an ultrafine-grained structure was formed.

3.3. Evolution of the deformation microstructure accompanying crack propagation

Local orientation analysis around the arrested intergranular crack in the uncharged specimen was performed using ACOM-TEM. Fig. 7(a) shows the ACOM-TEM orientation map superimposed on the STEM image near the blunted intergranular crack tip. The region around the crack was not preferentially etched, and the substructure around the

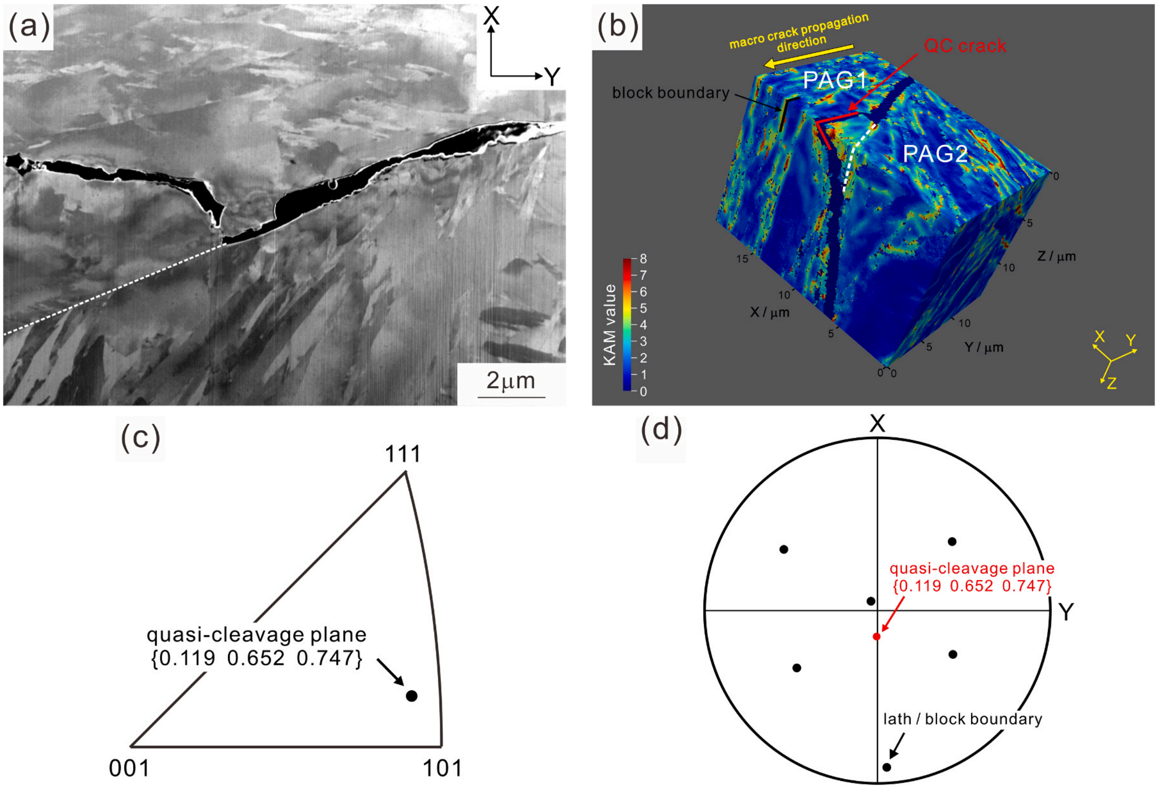

Fig. 5. (a) SEM image ($Z = 0$ μm), (b) 3D-EBSD KAM map, (c) stereographic triangle showing the orientation of the quasi-cleavage crack plane, and (d) <0 1 1> pole figure of the hydrogen-charged specimen with $H_D = 4.00$ wt ppm. The poles of the quasi-cleavage plane and lath / block boundaries are indicated in (d).

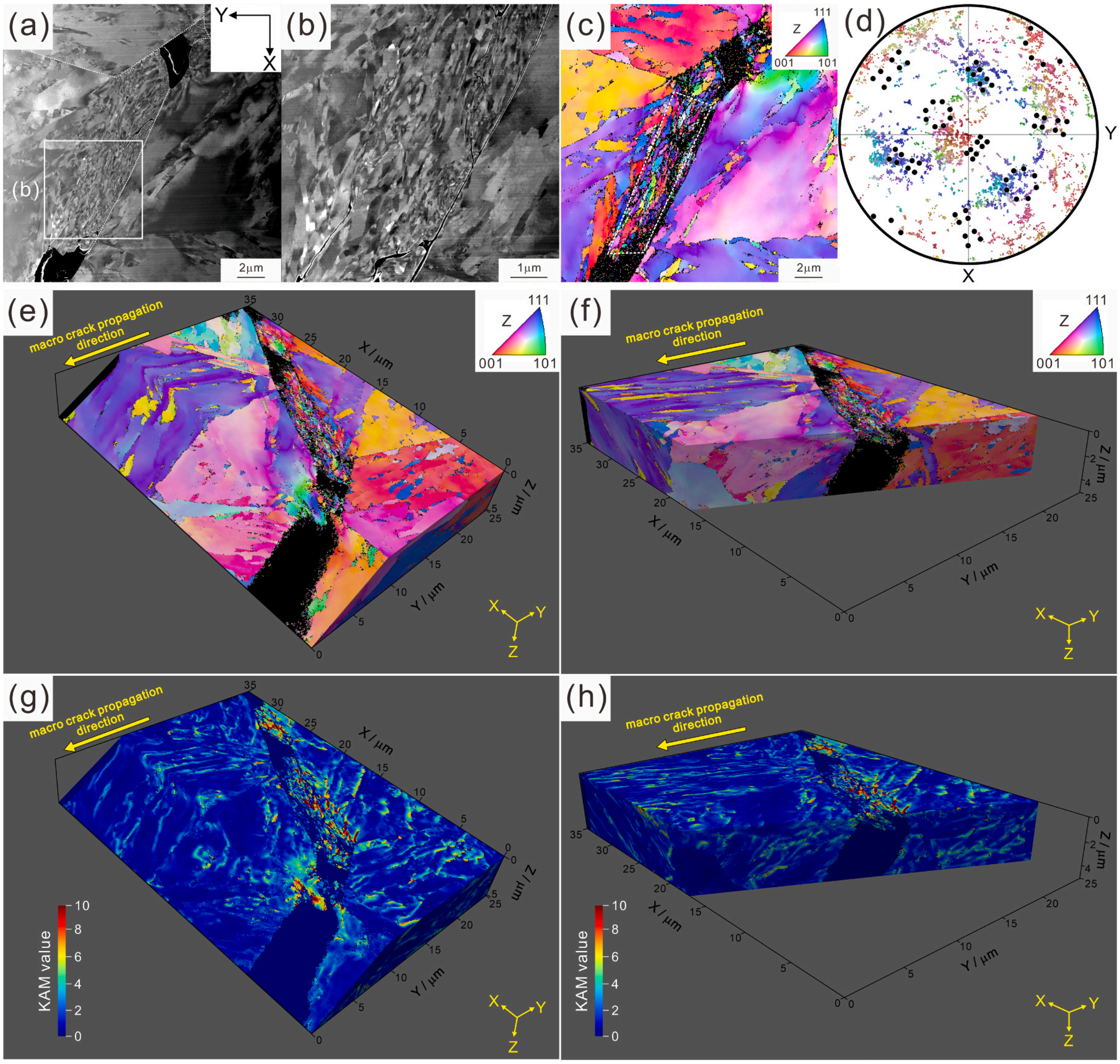

Fig. 6. (a, b) SEM images ($Z = 0$ μm), (c) EBSD orientation map ($Z = 0$ μm), (d) <0 0 1> pole figure of the white rectangular area in (c), on which the ideal poles of the 24 K-S variants are superimposed, (e, f) 3D-EBSD orientation maps, and (g, h) 3D-EBSD KAM maps of the hydrogen-charged specimen with $H_D = 4.00$ wt ppm.

crack can be clearly observed. The color indicates the crystal orientation parallel to the normal direction of the foil plane, and the local orientation tends to change around the blunted crack tip. Fig. 7(b) shows the misorientation profiles along lines 1, 2, and 3, whose positions are indicated in (a). No significant change in the crystal orientation is visible along lines 2 and 3, which are far from the crack. In contrast, the crystal orientation along line 1 changes gradually towards the blunted crack tip by up to 7 °. This indicates that plastic accommodation occurred over a relatively large area when the crack tip was blunted. Fig. 7(c – e) shows dark-field STEM images of (c) the region near the crack tip, (d) the region 5.65 μm away from the crack tip, and (e) the non-deformed (as heat-treated) state in the uncharged specimen. The observations were performed under a two-beam condition with a diffraction vector of $\boldsymbol{g}^* = 0\ 1\ 1$, as indicated by the diffraction patterns inserted at the upper-right corners. Many straight dislocations are observed in the region 5.65 μm away from the crack tip (Fig. 7(d)), which are similar in the non-deformed state (Fig. 7(e)). In contrast, the dislocations near the crack tip are more curved and tangled (Fig. 7(c)), indicating that plastic accommodation occurred when the crack tip was blunted. However, the deformation microstructure did not sufficiently develop. Fig. 7(f) summarizes the dislocation densities in each region. Although the dislocation density of the non-deformed specimen is 0.9×10^{15} m^{-2}, the dislocation density increases up to 1.7×10^{15} m^{-2} towards the crack tip. Even in the region 5.65 μm away from the crack tip, the dislocation density is 1.1×10^{15} m^{-2}, which is higher than that in the non-deformed specimen. This suggests that plastic accommodation associated with the blunting of the crack tip occurred over a relatively large region ranging several to tens of micrometers. The size of the plastic zone (r_p) estimated from fracture mechanics assuming the plane strain condition is derived using Eq.1 [60]:

$$r_p = \frac{1}{3\pi}\left(\frac{K}{\sigma_y}\right)^2 \tag{1}$$

where K is the stress intensity factor, and σ_y is the yield strength. The plastic zone estimated from the unloading compliance tests (K_Q = 49.4 MPa $\mathrm{m}^{1/2}$) is 306 μm, which is considerably larger than the size confirmed by the ACOM-TEM and STEM analyses (Fig. 7). This could be because intergranular fracture in martensitic steels does not correspond to a single main crack propagation, but results from many cracks propagating with frequent branching [30,54].

Fig. 8(a – c) shows the 3D crack morphology (blue: intergranular crack component and red: quasi-cleavage crack component) in the hydrogen-charged specimen with $H_D = 4.00$ wt ppm. In contrast to the 3D images shown in Figs. 3-6, the section of $Z = 0$ μm in Fig. 8 was set as

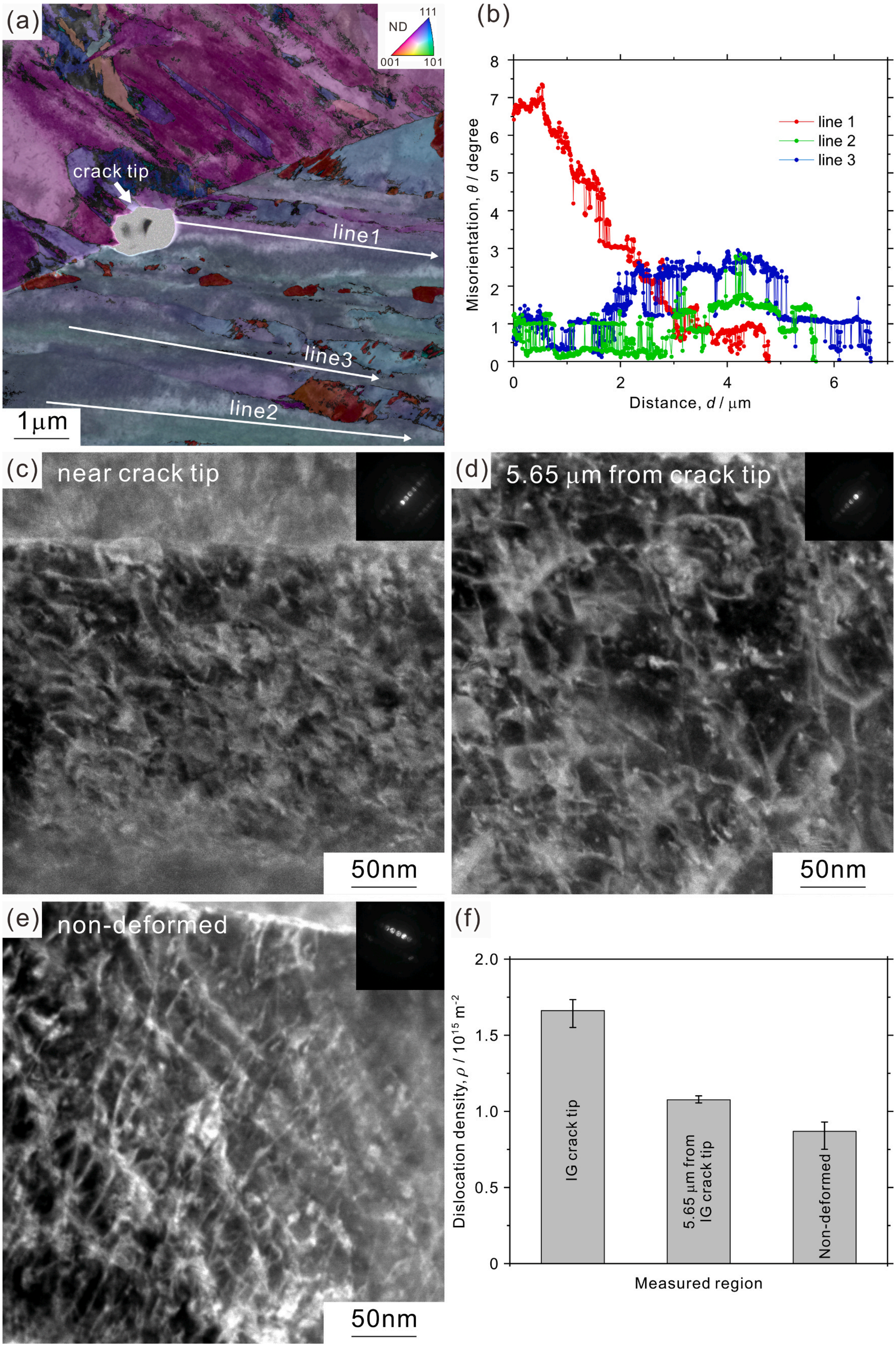

Fig. 7. (a) ACOM-TEM orientation map superimposed on the STEM image, (b) misorientation profiles along lines 1, 2, and 3, whose positions are indicated in (a), (c – e) dark-field STEM images ((c) near the crack tip, (d) 5.65 μm from the crack tip, and (e) non-deformed state), and (f) dislocation densities of each region in the uncharged specimen.

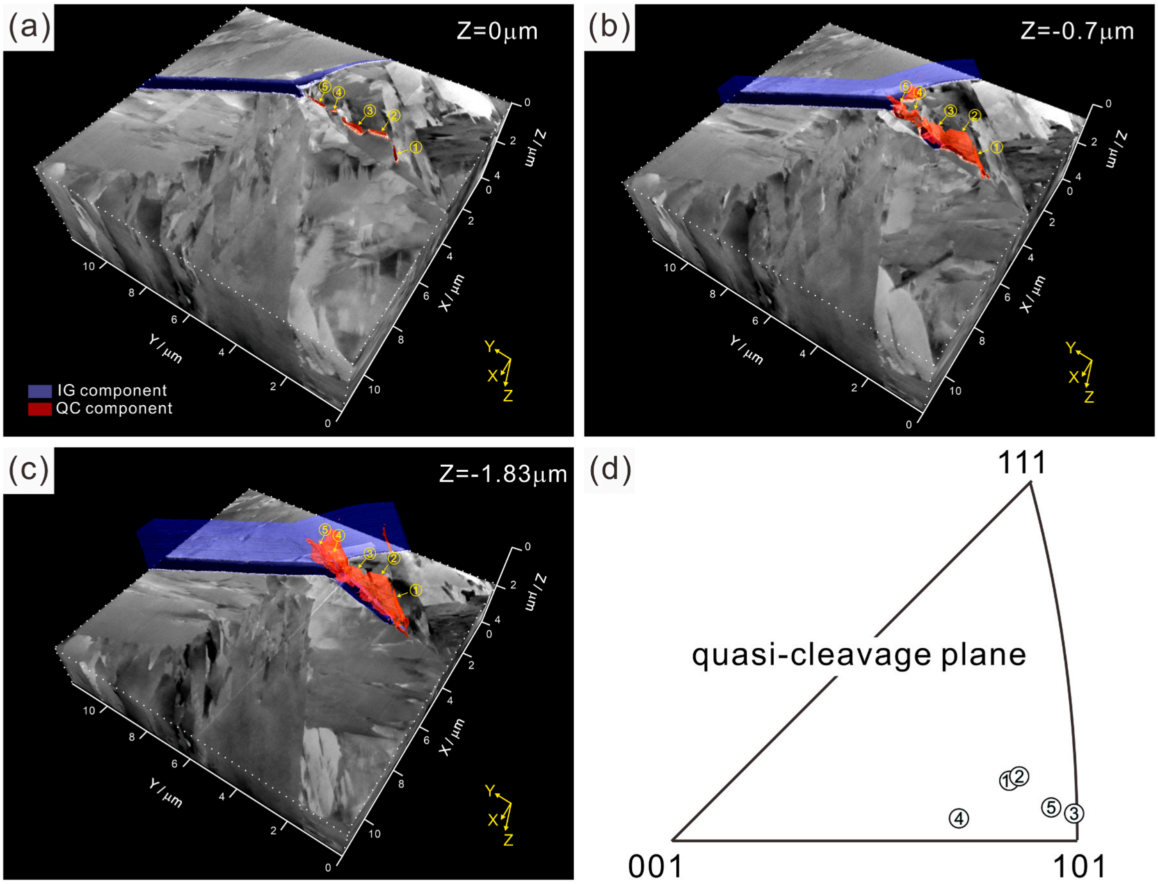

Fig. 8. (a – c) 3D crack morphology ((a) $Z = 0$ µm, (b) $Z = -0.7$ µm, and (c) $Z = -1.83$ µm (blue: intergranular crack component and red: quasi-cleavage crack component)) and (d) stereographic triangle showing the orientation of the microscopic quasi-cleavage crack facets of the hydrogen-charged specimen with $H_D =$ 4.00 wt ppm.

the final section in the FIB-SEM serial sectioning to easily understand the crack morphology. Several microscopic isolated quasi-cleavage cracks with different faceted planes (5 cracks in total) are observed at the region ahead of the intergranular crack in the section $Z = 0$ µm (Fig. 8(a)). However, as shown in the $Z = -0.7$ µm and $Z = -1.83$ µm sections (Fig. 8(b, c)), these cracks are fully interconnected in the region below the $Z = 0$ µm section. According to the 3D crack morphology, we find that the quasi-cleavage crack propagation is non-uniform changing microscopic faceted plane frequently. Fig. 8(d) shows the stereographic triangle indicating the normal directions of these microscopic facets determined by two-surface trace analysis (the number of each pole corresponds to that of the facet in (a) – (c)). It is clear that the facets are close to the {0 1 1} plane. However, the misorientation of some facets from the {0 1 1} plane is large (particularly, 12.46 ° for facet 4), indicating that the quasi-cleavage crack does not originate from atomistic decohesion at {0 1 1} plane. Fig. 9(a) shows a low-magnification STEM image around the crack, and the observed section is almost the same as the final section in the FIB-SEM serial sectioning (Fig. 8(a)). Although several studies reported that the quasi-cleavage cracks propagated at the lath boundaries [31–34], the high-magnification STEM images of Fig. 9

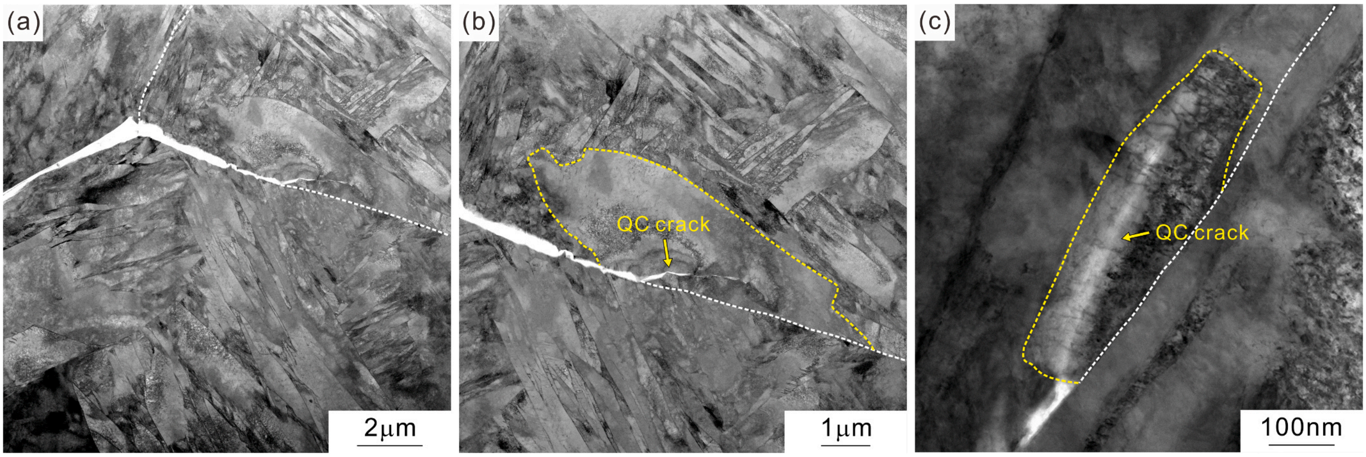

Fig. 9. STEM images of the hydrogen-charged specimen with $H_D = 4.00$ wt ppm.

(b, c) clearly demonstrate that the quasi-cleavage crack propagation occurred inside the lath and not at the lath boundaries (the positions of the lath boundaries are indicated by the yellow-dashed lines).

Fig. 10 (a) is an ACOM-TEM orientation map superimposed on the STEM image, and (b) is the local misorientation of the PAGB obtained from the orientation map of (a) in the hydrogen-charged specimen with $H_D = 4.00$ wt ppm. The crack deviated from the PAGB at position ‘A’ and propagated as a quasi-cleavage crack, as shown in Fig. 10 (c). In the region ahead of position ‘A’, a substantial portion of PAGB segments exhibit a misorientation of less than 10 °. Additionally, we can confirm the evidence of ductile rupture at position ‘B’ (Fig. 10 (d)). The misorientation of the PAGB segment at position ‘B’ is also small. Consequently, the crack propagation into the PAG interior and the ductile rupture occurred at the low-angle PAGB segments, indicating that the low-angle PAGB segments provide strong resistance to intergranular crack propagation.

The results of the local orientation analysis in the hydrogen-charged specimen with $H_D = 4.00$ wt ppm are shown in Fig. 11 ((a) ACOM-TEM orientation map superimposed on the STEM image and (b) misorientation profiles along lines 1 and 2 in (a)). The analyzed region corresponds to the area around the quasi-cleavage crack tip depicted in Fig. 10 (a). Although the misorientation along line 2, which is far from the crack, is approximately 2 °, the orientation changes significantly up to 10 ° towards the crack tip within 1 µm along line 1. Therefore, in the hydrogen-related quasi-cleavage fracture, plastic accommodation occurred in a localized region around the crack tip. Furthermore, the plastic accommodation region is considerably smaller than the plastic zone estimated using Eq. 1 (35 µm when using $K_Q = 16.7$ MPa $m^{1/2}$). The dark-field STEM images in the hydrogen-charged specimen with $H_D = 4.00$ wt ppm are shown in Fig. 12 ((a) the region near the quasi-cleavage crack tip, (b) the region 1.58 µm away from the quasi-cleavage crack, (c) the wake region of the quasi-cleavage crack, and (d) the wake region of the intergranular crack). In the vicinity of the quasi-cleavage crack tip, so-called low-energy dislocation structures (LEDS) as well as curved and tangled dislocations are observed (Fig. 12 (a)). In contrast, the microstructure in the region 1.58 µm away from the quasi-cleavage crack tip (Fig. 12 (b)) is similar to that of the non-deformed specimen (Fig. 7(e)). This is consistent with the orientation change significantly localized near the crack tip, as shown in Fig. 11. A well-developed deformation microstructure, that is, LEDS and curved / tangled dislocations, is also observed in the wake region of the quasi-cleavage crack (Fig. 12 (c)). This indicates that the hydrogen-related quasi-cleavage crack

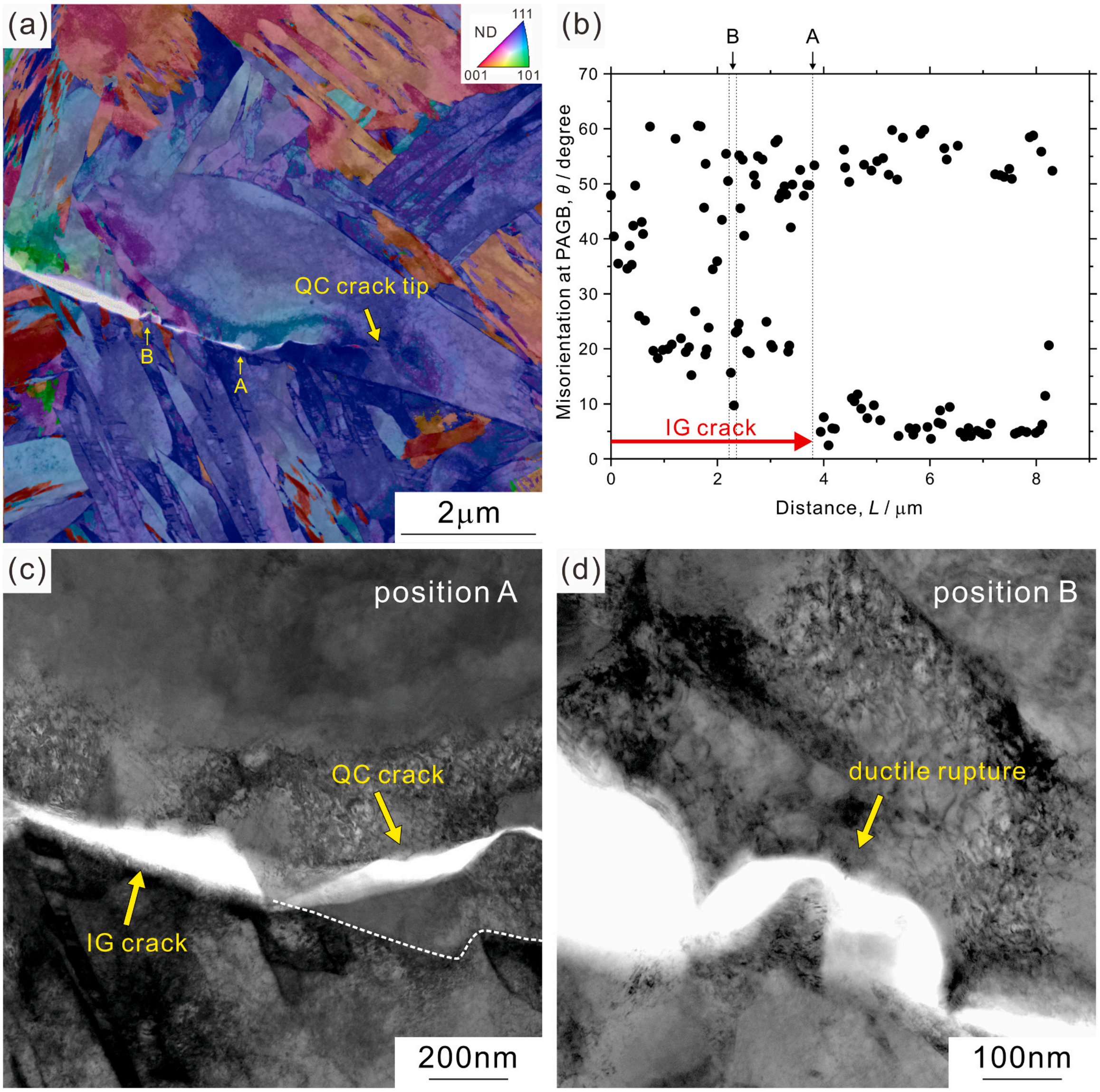

Fig. 10. (a) ACOM-TEM orientation map superimposed on the STEM image, (b) local misorientation of the prior austenite grain boundary, and (c, d) STEM images at positions A and B indicated in (a) in the hydrogen-charged specimen with $H_D = 4.00$ wt ppm.

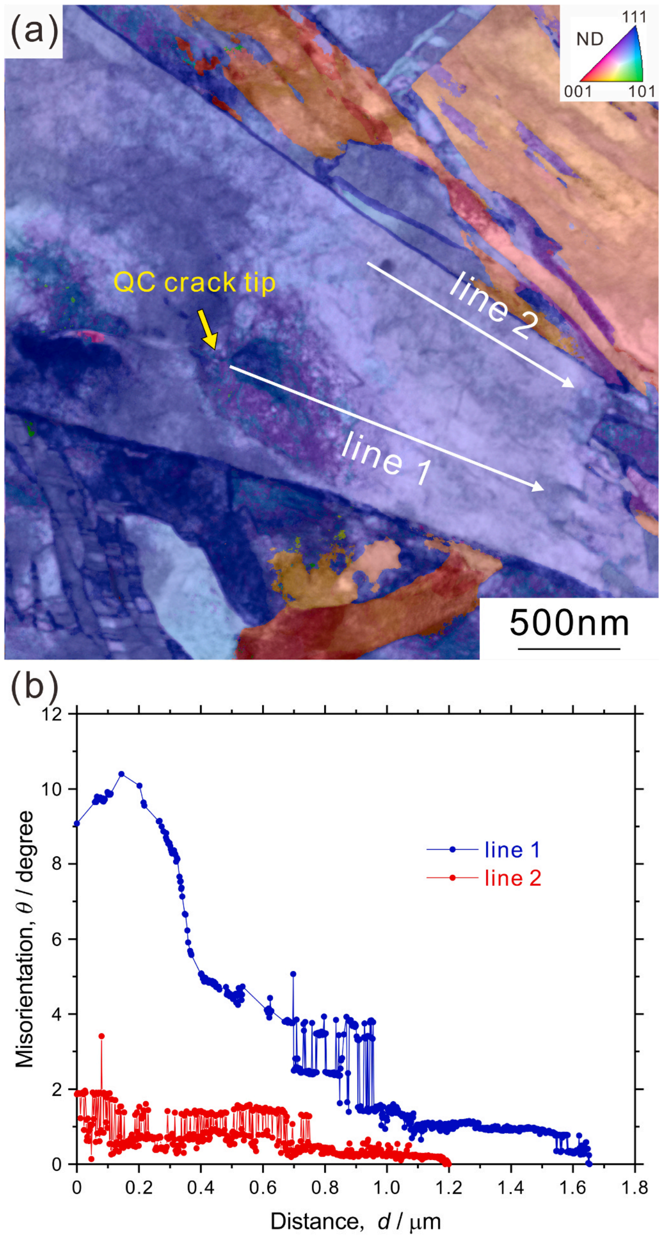

Fig. 11. (a) ACOM-TEM orientation map superimposed on the STEM image and (b) misorientation profiles along lines 1 and 2, whose positions are indicated in (a), in the hydrogen-charged specimen with H_D = 4.00 wt ppm.

propagation was accompanied by a remarkable evolution of the deformation microstructure. On the other hand, tangled dislocations are partially observed around the intergranular crack in Fig. 12 (d). Fig. 12 (e) summarizes the dislocation densities in each region. While the dislocation densities are high at the tip of the quasi-cleavage crack (1.5 $\times$ 10^{15} m^{-2}) and the wake region of the quasi-cleavage crack (1.4 $\times$ 10^{15} m^{-2}), the dislocation density at a distance of 1.58 μm from the crack tip decreases to 0.8 $\times$ 10^{15} m^{-2}, which is almost the same as that in the non-deformed specimen (0.9 $\times$ 10^{15} m^{-2}). Therefore, we can say that the plastic deformation was significantly localized in the vicinity of the quasi-cleavage crack from the viewpoint of dislocation densities. The dislocation density around the intergranular crack is 1.2 $\times$ 10^{15} m^{-2}, which is higher than that of the non-deformed specimen, indicating that the intergranular crack propagation was also accompanied by a certain amount of plastic deformation.

4. Discussion

4.1. Local plastic deformation behavior accompanying hydrogen-related crack propagation

The hydrogen-related quasi-cleavage crack propagation nearly parallel to the {0 1 1} planes was accompanied by local plastic deformation, as confirmed by the large KAM value in the 3D-EBSD KAM map shown in Fig. 5. In addition, despite the small macroscopic *J*-integral value in the hydrogen-charged specimen (Fig. 2), we demonstrated, based on the analysis of dislocation microstructures, local crystal orientation changes, and dislocation densities, that the evolution of the deformation microstructure ahead of the hydrogen-related quasi-cleavage crack was remarkable compared with that accompanying the intergranular crack in the uncharged specimen, as shown in Figs. 7, 11, and 12. Previously, we investigated the effect of hydrogen on the evolution of the deformation microstructure in a low-carbon steel with a simple microstructure consisting of ferrite and pearlite using neutron diffraction and STEM analyses [61]. The fraction of screw dislocations in the uncharged specimen was significantly large (approximately 97%) at the initial stage of deformation (e = 3%). This could be due to the relatively higher mobility of the non-screw dislocation segment in bcc crystal [62–66]. In contrast, the fractions of edge and screw dislocations at the initial stage of deformation (e = 3%) were comparable in the hydrogen-charged specimen. Moreover, the size of LEDS tended to be smaller and the misorientation of LEDS was larger in the hydrogen-charged specimen than those in the uncharged specimen [61]. This suggests that hydrogen increases the relative mobility of screw dislocations to edge dislocations (by either decreasing the mobility of edge dislocations or increasing the mobility of screw dislocations). The recent in-situ mechanical tests in TEM [67] and the molecular dynamics simulations [68] support this idea. Huang et al. [67] reported the enhanced screw dislocation motion in α-iron by analyzing the movement of each individual dislocation. Matsumoto et al. [68] performed the molecular dynamic simulations and revealed that the movement of edge dislocations was significantly suppressed as the hydrogen concentration increased. The high relative mobility of the screw dislocations leads to frequent cutting of screw dislocations. Accordingly, we can consider that the change in the dislocation characteristics (that is, the increased relative mobility of screw dislocations) results in the remarkable evolution of the deformation microstructure around the hydrogen-related quasi-cleavage crack observed in Fig. 12, which is consistent with the finding in the previous study indicating that hydrogen facilitates the evolution of the deformation microstructure in ferritic steel with a simple microstructure [61].

Fig. 13 presents a summary of the local misorientation and dislocation density around the crack tip based on the results shown in Figs. 7, 11, and 12. The misorientation and dislocation density are plotted as a function of the distance from the crack tip in the uncharged specimen (red) and the hydrogen-charged specimen with H_D = 4.00 wt ppm (blue). In the uncharged specimen, the orientation changes gradually towards the crack tip, and the dislocation density increases as the crack tip is approached. The dislocation density is higher than that of the non-deformed state, even at a distance of 5.65 μm from the crack tip, indicating that plastic accommodation occurred over a relatively large area. In the hydrogen-charged specimen, the orientation changes abruptly within 1 μm of the crack tip. The dislocation density is high near the crack tip, and deformation microstructures, such as LEDS formations, are developed. The dislocation density decreases abruptly at 1.58 μm from the crack tip and is almost the same as that in the non-deformed state. Therefore, the plastic accommodation region in the hydrogen-charged specimen is significantly smaller than that in the uncharged specimen. One possible reason for this is the difference in the macroscopic applied load (K_Q = 49.4 for the uncharged specimen and K_Q = 16.7 MPa $m^{1/2}$ for the hydrogen-charged specimen with H_D = 4.00 wt ppm (Fig. 2(b)). The plastic accommodation region in both the uncharged and hydrogen-charged specimens estimated from the STEM

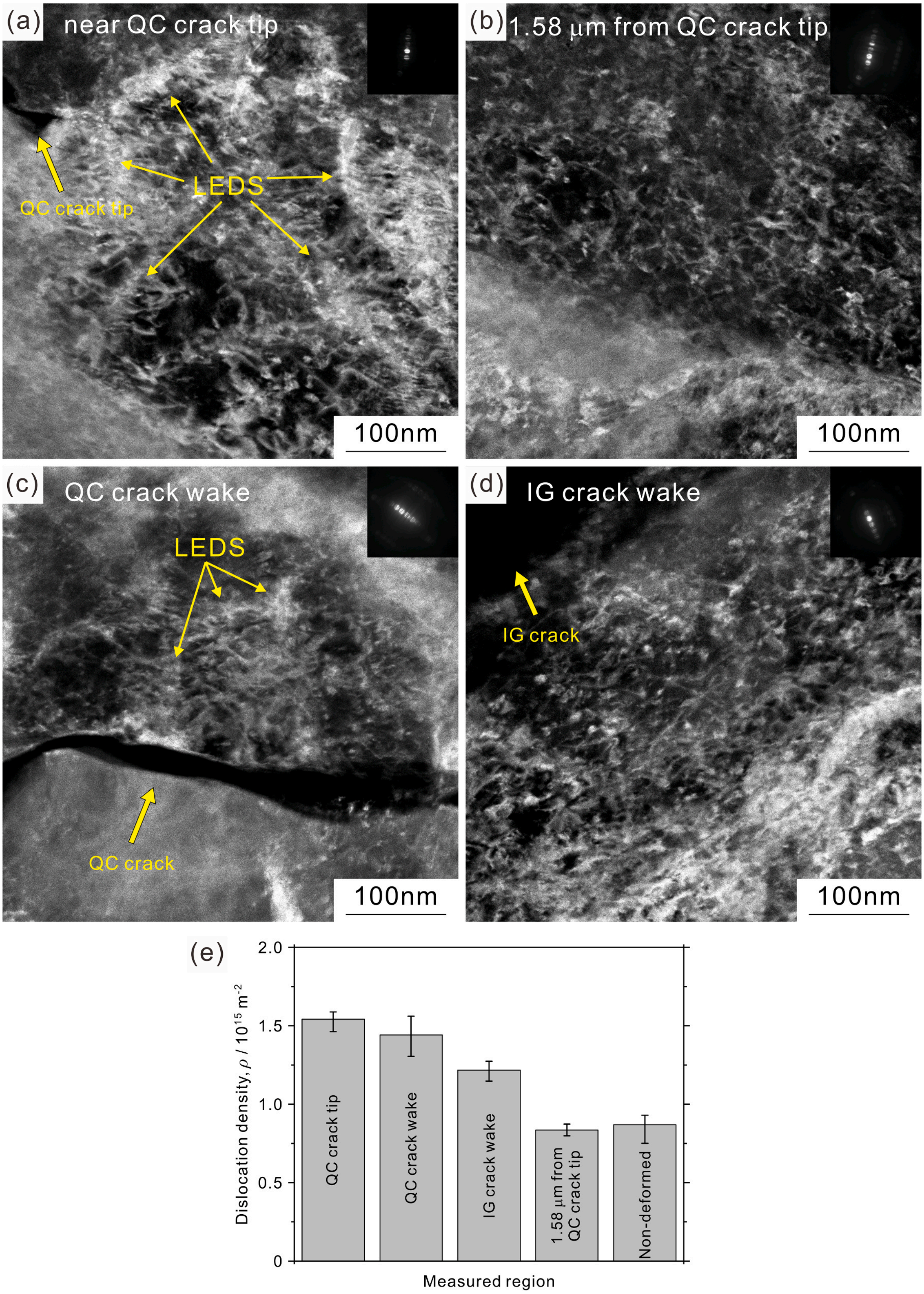

Fig. 12. (a – d) Dark-field STEM images ((a) near the quasi-cleavage crack tip, (b) 1.58 μm from the quasi-cleavage crack tip, (c) wake of the quasi-cleavage crack, and (d) wake of the intergranular crack), and (e) dislocation densities of each region in the hydrogen-charged specimen with $H_D = 4.00$ wt ppm.

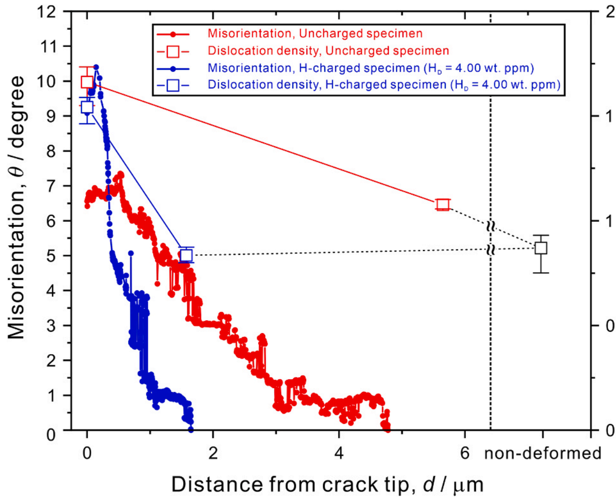

Fig. 13. Local misorientation and dislocation density plotted as a function of distance from the crack tip in the uncharged specimen (red) and the hydrogen-charged specimen with $H_D = 4.00$ wt ppm (blue).

analysis is approximately one-thirtieth of the plastic zone derived from fracture mechanics using Eq. 1. If the plastic accommodation around the crack tip depends only on the macroscopic applied load (stress intensity factor), the misorientation profile should have a similar shape. However, as shown in Fig. 13, the orientation change around the hydrogen-related quasi-cleavage crack is significantly greater than that of the uncharged specimen. Additionally, the development of deformation microstructures, such as LEDS formations, are remarkable in the hydrogen-charged specimen (Fig. 12). Therefore, we suggest that hydrogen induces intense strain localization around the crack tip. The hydrogen-related intergranular crack propagation also involves plastic deformation because the dislocation density around the intergranular crack is higher than that in the non-deformed state, as shown in Fig. 12. Moreover, plastic deformation sufficiently large to form an ultrafine-grained structure sometimes occurred locally at the tip of an arrested intergranular crack with a large opening displacement (Fig. 6). Therefore, we can conclude that intense local plastic deformation is involved in the hydrogen-related crack propagation (both quasi-cleavage and intergranular).

As described in the Section 1, the characteristics of quasi-cleavage fractures are controversial. To clarify whether the crack propagated at the lath boundaries or not, it is necessary to study cracks with small opening displacement by microstructure observations with high spatial resolution. Analysis of the fracture surfaces or largely opened cracks is insufficient because the lath width is very small. Because lath boundaries are low-angle boundaries (usually less than 3 ° [15]), special reasons are required to explain the preferential cracking / decohesion at lath boundaries rather than at block boundaries, packet boundaries, and PAGBs, many of which are high-angle boundaries. Matsumoto et al. [69] investigated the cohesive energies of <1 1 0> symmetrical tilt grain boundaries with different misorientation angles in pure iron under a gaseous hydrogen environment using density function theory calculations. According to their calculation results, the reduction in the cohesive energy owing to hydrogen was more pronounced at higher-energy (higher-angle) grain boundaries. If quasi-cleavage cracking is due to boundary decohesion, the cracks occasionally formed at the lath boundaries should change their propagation path to the PAGBs (or other high-angle boundaries) when they reach the PAGBs (or other high-angle boundaries). In addition to the previous studies [35,36], the results shown in Figs. 5 and 9 conclusively demonstrate that the quasi-cleavage crack propagated inside the lath and not at the lath boundaries. The formation of serrated markings (or tear ridges) on the resulting fracture surface, which are different from the river patterns on cleavage surface, is one of the important characteristics of hydrogen-related quasi-cleavage fracture. However, it is sometimes difficult to distinguish between conventional cleavage fractures and quasi-cleavage fractures from the perspective of fracture surface morphology. The results shown in Figs. 5 and 8 clearly indicate that the quasi-cleavage crack planes, even microscopic facet planes, are close to the {0 1 1} plane and not to the {0 0 1} plane. Because several studies have reported that hydrogen also promotes cleavage fracture [34,48,49,70], hydrogen-related transgranular fractures with crack planes parallel to the {0 0 1} could be classified as cleavage fractures rather than quasi-cleavage fractures. Considering that quasi-cleavage fracture also occurs along the {0 1 1} plane in ferritic steel with a simple microstructure [38], we can propose that fracture along the {0 1 1} plane is one of the most important features for characterizing hydrogen-related quasi-cleavage fractures in steels with bcc phases.

Because the crack planes depicted in Figs. 5 and 8 do not exactly align with the {0 1 1} plane, the quasi-cleavage fracture is not originated from atomistic cleavage fracture at the {0 1 1} plane. Though further studies should be necessary, one potential scenario of the hydrogen-related quasi-cleavage fracture is as follows. The high relative mobility of the screw dislocations results in the remarkable evolution of deformation microstructure by frequent cutting of screw dislocations (Figs. 11 and 12), consequently leading to the persistent generation of vacancies. First-principles calculations [71] have indicated that hydrogen increased the activation energy for vacancy diffusion, thereby reducing diffusivity of vacancies. As a result, the vacancies nucleated by jog-dragging of screw dislocations remained at a high density in the vicinity of the slip planes. Consequently, we can propose that the remaining high-density vacancies or nanovoids coalesced with each other, leading to a hydrogen-related quasi-cleavage fracture.

4.2. *Crack propagation behavior and its relationship to the macroscopic mechanical response*

As illustrated in Fig. 4, hydrogen-related intergranular fracture predominantly occurs at PAGBs, though there are several types of high-angle boundaries in lath martensite structure, including block boundaries and packet boundaries. Previously, hydrogen microprint analysis revealed that deformation enhanced accumulation of hydrogen around the PAGBs [72,73]. We can propose three potential explanations for preferential hydrogen accumulation leading to intergranular cracking at PAGBs; (i) segregation of impurities, (ii) coherency, and (iii) stress/strain concentration. (i) Because the boundaries in martensite other than PAGB are formed during quenching, we can expect that segregation of impurities at PAGB is significantly higher compared to the other boundaries. The segregated impurities at PAGBs could facilitate their interaction with hydrogen, leading to the preferential accumulation of hydrogen at PAGBs. (ii) The boundaries other than PAGB are basically variant boundaries with a definite crystallographic orientation relationship. In contrast, PAGB is a kind of random boundary. Consequently, the coherency of PAGB is lower, resulting in a larger amount of free volume. This lower coherency makes PAGBs prone to the accumulation of hydrogen. (iii) Although previous studies reported that the most effective boundary for strength in martensitic steel is block boundary [74,75], we can speculate that large stress/strain concentrations arise around PAGBs during deformation. The low crystallographic coherency of PAGB could also increase stress/strain accumulation due to low slip compatibility. As hydrogen tends to accumulate around high stress/strain regions [76–78], PAGBs become preferential trapping site of hydrogen.

In addition to the previous studies [30,47], the results shown in Figs. 3, 4 and 10 clearly demonstrate that the low-angle PAGB segments impeded intergranular crack propagation. Here, we discuss the effect of low-angle PAGB segments with a relatively small size on intergranular crack propagation (Fig. 14 (a, b)). For the uncharged specimen, the crack propagates under a large load, and the stress concentration area around the crack tip is large. Therefore, even when the crack reaches a

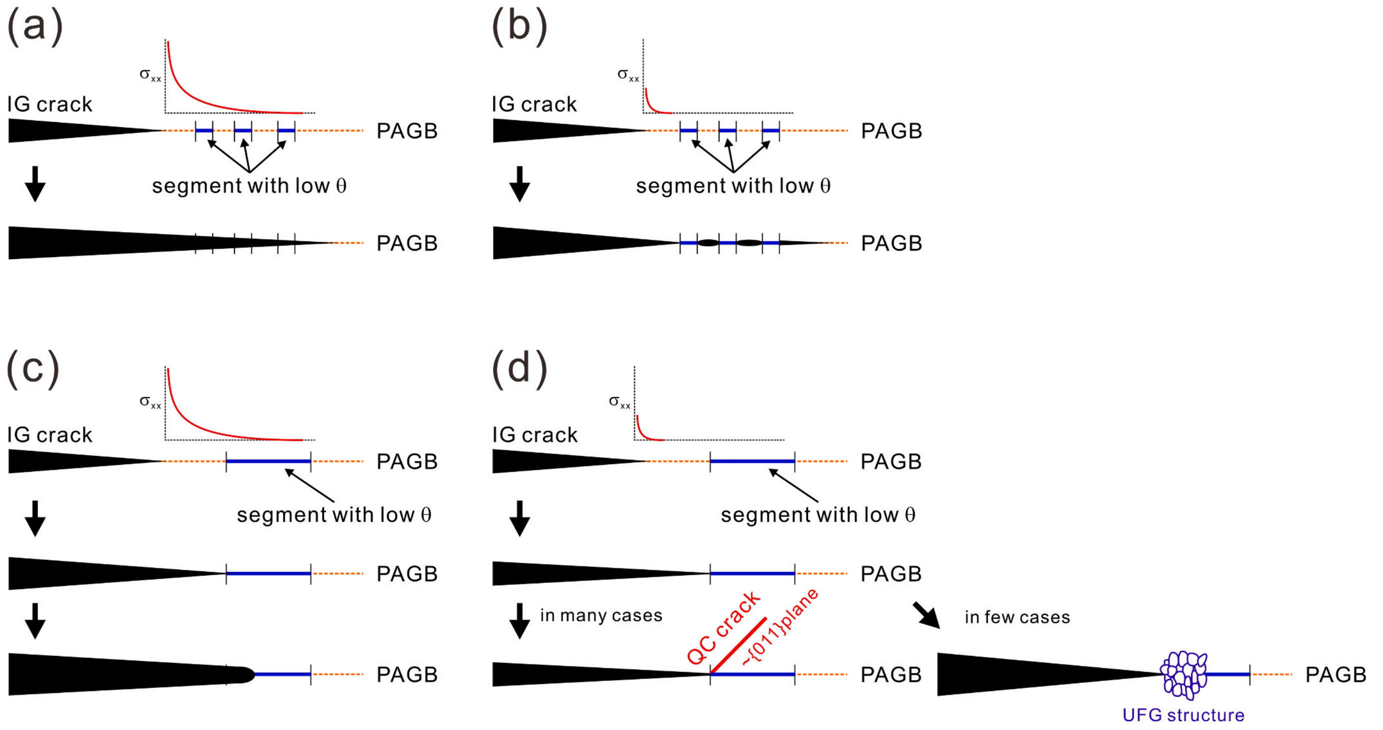

Fig. 14. Schematic illustration showing the effect of a low-angle boundary segment on the crack propagation in the (a, c) uncharged specimen and (b, d) hydrogen-charged specimen.

low-angle PAGB segment with a small size, it has little effect on the crack propagation, resulting in continuous crack propagation (Fig. 14 (a)). For the hydrogen-charged specimen, even when the size of the low-angle PAGB segment is small, the segment can impede crack propagation owing to the small stress concentration range (Fig. 14 (b)). Furthermore, this behavior is also associated with the hydrogen accumulation behavior. Previously, hydrogen microprint analysis indicated that deformation promoted hydrogen accumulation around the PAGBs [72, 73]. Generally, the segregation of impurities at the grain boundary decreases as the grain boundary misorientation decreases [79]. Although the local hydrogen distribution is difficult to quantitatively evaluate (in particular, the distribution of diffusible hydrogen), it can be speculated that the local concentration of hydrogen around the low-angle PAGB segments is expected to be lower than that around the high-angle PAGB segments. The low hydrogen concentration could suppress the degradation of the cohesive energy of the PAGB segments. As described above, the reduction in the cohesive energy by hydrogen is more pronounced at the higher-energy grain boundaries [69]. Namely, the presence of hydrogen increases the difference in the cohesive energy between low-angle and high-angle PAGB segments. Therefore, the high-angle PAGB segments are preferentially cracked, while the low-angle PAGB segments still exhibit high resistance to cracking, leading to discontinuous crack propagation as shown in Fig. 4. This could elucidate why even low-angle PAGB segments with small size, specifically sub-micrometer size, can impede the propagation of hydrogen-related crack. As shown in Fig. 1, sulfur is segregated in the PAGB. If the main reason for the discontinuous crack propagation is sulfur segregation depending on grain boundary character, intergranular crack propagation behavior should be the same between the uncharged specimen and hydrogen-charged specimen. Because the obstacle effect of low-angle PAGB segments with a small size can be observed only in the hydrogen-charged specimen, it is reasonable to consider that the presence of hydrogen played a primary role on the crack propagation behavior depicted in Fig. 4.

Next, we discuss the effect of low-angle PAGB segments that are relatively large in size (Fig. 14 (c, d)). In both uncharged and hydrogen-charged specimens, the low-angle PAGB segment with a relatively large size impedes crack propagation. Plastic accommodation and resultant crack tip blunting occur in the uncharged specimen (Fig. 14 (c)). The crack tip blunting increases the resistance to crack propagation, resulting in the arrest of the crack. The un-cracked ligaments are then fractured in a ductile manner at a later fracture process. For the hydrogen-charged specimen, even if the size of the low-angle PAGB segment is sufficiently large to prevent crack propagation, obvious crack tip blunting does not occur [47]. In many cases, the crack can continue propagating inside the PAG in a quasi-cleavage manner (Fig. 14 (d)). The propagation of the quasi-cleavage cracks is accompanied by the development of pronounced deformation microstructures (Fig. 12). In other words, cracks can propagate within the PAG even after the intergranular crack propagation has stopped. When the crack reaches another PAGB, it propagates again in an intergranular manner. On the contrary, when the arrested intergranular crack cannot propagate further within the grain as a quasi-cleavage crack, resulting in a notably large opening displacement in the wake region, plastic deformation large enough to form an ultrafine-grained structure occurs at the arrested crack tip (Figs. 6 and 14 (d)). Accordingly, we can propose that, due to the intense localized plastic work involved in the arrest of intergranular cracks (Fig. 6) and the propagation of quasi-cleavage cracks (Figs. 11 and 12), there exists a certain degree of resistance to crack propagation (intrinsic crack growth resistance), even in the case of high hydrogen concentrations (Fig. 2).

Based on the findings presented in this paper, we suggest that the martensite microstructure with a large fraction of low-angle PAGB segments could mitigate hydrogen-related intergranular fracture. Controlling the martensitic transformation, particularly through variant selection at austenite grain boundaries during the nucleation stage, would be crucial in achieving the optimal microstructure for enhanced resistance to hydrogen embrittlement.

5. Conclusions

We investigated the hydrogen-related crack propagation behavior and evolution of the deformation microstructure associated with crack propagation in high-strength martensitic steel using FIB-SEM serial sectioning and TEM analysis. The following conclusions were drawn.

(1) For the uncharged specimen, the intergranular crack was arrested at low-angle PAGB segments with a size of several micrometers. The crystallographic orientation gradually changed towards the crack tip, and the dislocation density was higher than that in the non-deformed state, even at a distance of approximately 5.65 μm from the crack tip. This indicates that plastic accommodation associated with the blunting of the crack tip occurred over a relatively large region ranging several to tens of micrometers.
(2) Even when the size of low-angle PAGB segment was small, it could act as an obstacle to hydrogen-related crack propagation. This could be because hydrogen increased the difference in cohesive energy between the low-angle and high-angle PAGB segments. After the intergranular crack was arrested, the crack continued to propagate into the grain interior as a quasi-cleavage crack. Additionally, plastic deformation sufficiently large to form an ultrafine-grained structure sometimes occurred locally at the tip of the arrested intergranular crack.
(3) The crystallographic orientation changed abruptly within 1 μm of the hydrogen-related quasi-cleavage crack tip. The dislocation density at the hydrogen-related quasi-cleavage crack tip was high, and deformation microstructures, such as LEDS, developed remarkably. The dislocation density around the hydrogen-related intergranular crack was also higher than that in the non-deformed state.
(4) The crystallographic analysis clearly indicated that the quasi-cleavage crack planes, even microscopic facet planes, were close to the {0 1 1} plane (but not exactly align with the {0 1 1} plane) rather than the {0 0 1} plane. Furthermore, the {0 1 1} plane near the quasi-cleavage fracture differed from the {0 1 1} plane parallel to the lath and block boundaries. On this basis, we concluded that the quasi-cleavage fracture did not originate from either atomistic cleavage fracture or decohesion at the lath / block boundaries.
(5) Based on our comprehensive and precise analysis of the crack propagation behavior and deformation microstructures, we concluded that intense local plastic deformation significantly contributed to the hydrogen-related crack propagation. The presence of a certain degree of crack-growth resistance in the hydrogen-related fracture, as confirmed by fracture mechanics tests, could be attributed to the intense localized plastic work involved in arresting the intergranular crack and propagation of the quasi-cleavage crack.

CRediT authorship contribution statement

Akinobu Shibata: Writing – original draft, Project administration, Methodology, Investigation, Funding acquisition, Formal analysis, Conceptualization. **Ivan Gutierrez-Urrutia:** Writing – review & editing, Validation, Methodology. **Akiko Nakamura:** Visualization, Methodology, Investigation, Data curation. **Taku Moronaga:** Visualization, Methodology, Investigation, Data curation. **Kazuho Okada:** Writing – review & editing, Validation, Investigation. **Yazid Madi:** Writing – review & editing, Validation, Investigation. **Jacques Besson:** Writing – review & editing, Validation. **Toru Hara:** Writing – review & editing, Validation.

Declaration of Competing Interest

The authors declare that they have no known competing financial interests or personal relationships that could have appeared to influence the work reported in this paper

Data availability

The raw and processed data required to reproduce these findings cannot be shared at this time as the data also forms part of an ongoing study.

Acknowledgments

This work was financially supported by JST PRESTO (Grant Number JPMJPR2096), JSPS KAKENHI (Grant Numbers JP22K18910 and JP23H01717), and MEXT Program: Data Creation and Utilization Type Material Research and Development Project Grant Number JPMXP1122684766.

References

[1] R.A. Oriani, P.H. Josephic, Equilibrium aspects of hydrogen-induced cracking of steels, Acta Met. 22 (1974) 1065–1074.
[2] W.W. Gerberich, Y.Y. Chen, Hydrogen-controlled cracking - an approach to threshold stress intensity, Metall. Trans. A 65A (1975) 271–278.
[3] R.A. Oriani, P.H. Josephic, Equilibrium and kinetic studies of the hydrogen-assisted cracking of steel, Acta Met. 25 (1977) 979–988.
[4] C.D. Beachem, A new model for hydrogen-assisted cracking (hydrogen "embrittlement"), Metall. Trans. 3 (1972) 437–451.
[5] H.K. Birnbaum, P. Sofronis, Hydrogen-enhanced localized plasticity - a mechanism for hydrogen-related fracture, Mater. Sci. Eng. A 176 (1994) 191–202.
[6] P.J. Ferreira, I.M. Robertson, H.K. Birnbaum, Hydrogen effects on the interaction between dislocations, Acta Mater. 46 (1998) 1749–1757.
[7] I.M. Robertson, The effect of hydrogen on dislocation dynamics, Eng. Fract. Mech. 64 (1999) 649–673.
[8] S. Lynch, Hydrogen embrittlement phenomena and mechanisms, Corros. Rev. 30 (2012) 105–123.
[9] M. Nagumo, Function of hydrogen in embrittlement of high-strength steels, ISIJ Int 41 (2001) 590–598.
[10] M. Nagumo, H. Matsuda, Function of hydrogen in intergranular fracture of martensitic steels, Philos. Mag. A 82 (2002) 3415–3425.
[11] D. Guedes, L. Cupertino Malheiros, A. Oudriss, S. Cohendoz, J. Bouhattate, J. Creus, F. Thébault, M. Piette, X. Feaugas, The role of plasticity and hydrogen flux in the fracture of a tempered martensitic steel: a new design of mechanical test until fracture to separate the influence of mobile from deeply trapped hydrogen, Acta Mater. 186 (2020) 133–148.
[12] A.R. Marder, G. Krauss, The morphology of martensite in iron-carbon alloys, Trans. ASM 60 (1967) 651–660.
[13] J.M. Marder, A.R. Marder, The morphology of iron-nickel massive martensite, Trans. ASM 62 (1969) 1–10.
[14] S. Morito, H. Tanaka, R. Konishi, T. Furuhara, T. Maki, The morphology and crystallography of lath martensite in Fe-C alloys, Acta Mater. 51 (2003) 1789–1799.
[15] S. Morito, X. Huang, T. Furuhara, T. Maki, N. Hansen, The morphology and crystallography of lath martensite in alloy steels, Acta Mater. 54 (2006) 5323–5331.
[16] C.C. Kinney, K.R. Pytlewski, A.G. Khachaturyan, J.W. Morris, The microstructure of lath martensite in quenched 9Ni steel, Acta Mater. 69 (2014) 372–385.
[17] A. Shibata, G. Miyamoto, S. Morito, A. Nakamura, T. Moronaga, H. Kitano, I. Gutierrez-Urrutia, T. Hara, K. Tsuzaki, Substructure and crystallography of lath martensite in as-quenched interstitial-free steel and low-carbon steel, Acta Mater. 246 (2023) 118675.
[18] S. Morito, J. Nishikawa, T. Maki, Dislocation density within lath martensite in Fe-C and Fe-Ni alloys, ISIJ Int 43 (2003) 1475–1477.
[19] S.K. Banerji, C.J. McMahon Jr, H.C. Feng, Intergranular fracture in 4340-type steels: effects of impurities and hydrogen, Metall. Mater. Trans. A 9A (1978) 237–247.
[20] B. Craig, G. Krauss, The structure of tempered martensite and its susceptibility to hydrogen stress cracking, Metall, Mater. Trans. A 11A (1980) 1799–1808.
[21] M. Wang, E. Akiyama, K. Tsuzaki, Effect of hydrogen and stress concentration on the notch tensile strength of AISI 4135 steel, Mater. Sci. Eng. A 398 (2005) 37–46.
[22] R. Thodla, M.T. Piza Paes, B. Gerst, Hydrogen assisted cracking of AISI 4137M steel in O&G environments, Int. J. Hydro. Energy 40 (2015) 17051–17064.
[23] A. Shibata, T. Murata, H. Takahashi, T. Matsuoka, N. Tsuji, Characterization of hydrogen-related fracture behavior in as-quenched low-carbon martensitic steel and tempered medium-carbon martensitic steel, Metall. Mater. Trans. A 46A (2015) 5685–5696.
[24] A. Lyu, J. Lee, J.H. Nam, M. Kim, Y.K. Lee, Hydrogen absorption and embrittlement of martensitic medium-Mn steels, Corros. Sci. 221 (2023) 111304.
[25] G. Wang, Y. Yan, J. Li, J. Huang, Y. Su, L. Qiao, Hydrogen embrittlement assessment of ultra-high strength steel 30CrMnSiNi$_2$, Corros. Sci. 77 (2013) 273–280.
[26] P. Zhang, M. Laleh, A.E. Hughes, R.K.W. Marceau, T. Hilditch, M.Y. Tan, Effect of microstructure on hydrogen embrittlement and hydrogen-induced cracking behaviour of a high-strength pipeline steel weldment, Corros. Sci. 227 (2024) 11764.

[27] M. Ueda, H.Y. Yasuda, Y. Umakoshi, Effect of grain boundary character on the martensitic transformation in Fe–32at%Ni bicrystals, Acta Mater. 49 (2001) 3421–3432.

[28] M. Ueda, H.Y. Yasuda, Y. Umakoshi, Stress-induced martensitic transformation in Fe–Ni bicrystals, Acta Mater. 49 (2001) 4251–4258.

[29] M. Ueda, H.Y. Yasuda, Y. Umakoshi, Controlling factor for nucleation of martensite at grain boundary in Fe-Ni bicrystals, Acta Mater. 51 (2003) 1007–1017.

[30] A. Shibata, I. Gutierrez-Urrutia, A. Nakamura, G. Miyamoto, Y. Madi, J. Besson, T. Hara, K. Tsuzaki, Multi-scale three-dimensional analysis on local arrestability of intergranular crack in high-strength martensitic steel, Acta Mater. 234 (2022) 118053.

[31] Y.H. Kim, J.W. Morris Jr, The nature of quasicleavage fracture in tempered 5.5Ni steel after hydrogen charging, Metal. Mater. Trans. A 14A (1983) 1883–1888.

[32] A. Nagao, C.D. Smith, M. Dadfarnia, P. Sofronis, I.M. Robertson, The role of hydrogen in hydrogen embrittlement fracture of lath martensitic steel, Acta Mater. 60 (2012) 5182–5189.

[33] G.L. Pioszak, R.P. Gangloff, Hydrogen environment assisted cracking of modern ultra-high strength martensitic steels, Metall. Mater. Trans. A 48A (2017) 4025–4045.

[34] L. Cho, P.E. Bradley, D.S. Lauria, M.L. Martin, M.J. Connolly, J.T. Benzing, E.J. Seo, K.O. Findley, J.G. Speer, A.J. Slifka, Characteristics and mechanisms of hydrogen-induced quasi-cleavage fracture of lath martensitic steel, Acta Mater. 206 (2021) 116635.

[35] A. Shibata, Y. Momotani, T. Murata, T. Matsuoka, M. Tsuboi, N. Tsuji, Microstructural and crystallographic features of hydrogen-related fracture in lath martensitic steels, Mater. Sci. Technol. 33 (2017) 1524–1532.

[36] A. Shibata, T. Yonemura, Y. Momotani, M.-H. Park, S. Takagi, Y. Madi, J. Besson, N. Tsuji, Effects of local stress, strain, and hydrogen content on hydrogen-related fracture behavior in low-carbon martensitic steel, Acta Mater. 210 (2021) 116828.

[37] A. Shibata, H. Takahashi, N. Tsuji, Microstructural and crystallographic features of hydrogen-related crack propagation in low carbon martensitic steel, ISIJ Int 52 (2012) 208–212.

[38] K. Okada, A. Shibata, Y. Takeda, N. Tsuji, Crystallographic feature of hydrogen-related fracture in 2Mn-0.1C ferritic steel, Int. J. Hydro. Energy 43 (2018) 11298–11306.

[39] W. Wu, S. Liu, W. Li, J. Li, Identification of microstructure factors affecting hydrogen embrittlement of a 2205 duplex stainless steel, Corros. Sci. 208 (2022) 110643.

[40] X. Xing, Z. Pang, H. Zhang, J. Liu, G. Cui, Study of temperature effect on hydrogen embrittlement in X70 pipeline steel, Corros. Sci. 230 (2024) 111939.

[41] C.D. Beachem, Orientation of cleavage facets in tempered martensite (quasi-cleavage) by single surface trace analysis, Metall. Trans. 4 (1973) 1999–2000.

[42] J. Bestautte, S. Kalácska, D. Béchet, Z. Obadia, F. Christien, Investigation of quasi-cleavage in a hydrogen charged maraging stainless steel, Corros. Sci. 218 (2023) 111163.

[43] Y. Takeda, C.J. McMahon Jr, Strain controlled vs stress controlled hydrogen induced fracture in a quenched and tempered steel, Metall. Mater. Trans. A 12A (1981) 1255–1266.

[44] D.J. Rowenhorst, A. Gupta, C.R. Feng, G. Spanos, 3D crystallographic and morphological analysis of coarse martensite: combining EBSD and serial sectioning, Scr. Mater. 55 (2006) 11–16.

[45] S. Zaefferer, S.I. Wright, D. Raabe, Three-dimensional orientation microscopy in a focused ion beam–scanning electron microscope: a new dimension of microstructure characterization, Metall. Mater. Trans. A 39A (2008) 374–389.

[46] S. Zaefferer, S.I. Wright, Three-dimensional orientation microscopy by serial sectioning and EBSD-based orientation mapping in a FIB-SEM, in: A. Schwartz, M. Kumar, B. Adams, D. Field (Eds.), Electron Backscatter Diffraction in Materials Science, Springer, Boston, MA, 2009, pp. 109–122.

[47] A. Shibata, I. Gutierrez-Urrutia, A. Nakamura, K. Okada, G. Miyamoto, Y. Madi, J. Besson, T. Hara, K. Tsuzaki, Three-dimensional propagation behavior of hydrogen-related intergranular cracks in high-strength martensitic steel, Int. J. Hydro. Energy 48 (2023) 34565–34574.

[48] Y. Ogawa, D. Birenis, H. Matsunaga, A. Thøgersen, Ø. Prytz, O. Takakuwa, J. Yamabe, Multi-scale observation of hydrogen-induced, localized plastic deformation in fatigue-crack propagation in a pure iron, Scr. Mater. 140 (2017) 13–17.

[49] D. Birenis, Y. Ogawa, H. Matsunaga, O. Takakuwa, J. Yamabe, Ø. Prytz, A. Thøgersen, Interpretation of hydrogen-assisted fatigue crack propagation in BCC iron based on dislocation structure evolution around the crack wake, Acta Mater. 156 (2018) 245–253.

[50] T. Chen, M. Koyama, Y. Ogawa, H. Matsunaga, E. Akiyama, Martensite boundary characteristics on cycle- and time-dependent fatigue crack growth paths of tempered lath martensitic steels in a 90 MPa gaseous hydrogen atmosphere, Metall. Mater. Trans. A 54A (2023) 2512–2518.

[51] A. Shibata, I. Gutierrez-Urrutia, K. Okada, G. Miyamoto, Y. Madi, J. Besson, K. Tsuzaki, Relationship between mechanical response and microscopic crack propagation behavior of hydrogen-related intergranular fracture in as-quenched martensitic steel, Mater. Sci. Eng. A 831 (2022) 142288.

[52] ASTM E1820-17 Standard Test Method for Measurement of Fracture Toughness, 2017.

[53] Y. Bhandari, S. Sarkar, M. Groeber, M.D. Uchic, D.M. Dimiduk, S. Ghosh, 3D polycrystalline microstructure reconstruction from FIB generated serial sections for FE analysis, Comp. Mater. Sci. 41 (2007) 222–235.

[54] A. Shibata, Y. Madi, J. Besson, A. Nakamura, T. Moronaga, K. Okada, I. Gutierrez-Urrutia, T. Hara, Relationship between three-dimensional crack morphology and macroscopic mechanical properties of hydrogen-related fracture in martensitic steel, ISIJ Int 64 (2024) 660–667.

[55] D. Bika, J.A. Pfaendtner, M. Menyhard, C.J. McMahon Jr, Sulfur-induced dynamic embrittlement in a low-alloy steel, Acta Metall. Mater. 43 (1995) 1895–1908.

[56] M. Yamaguchi, First-principles study on the grain boundary embrittlement of metals by solute segregation: part I. iron (Fe)-solute (B, C, P, and S) systems, Metall. Mater. Trans. A 42A (2011) 319–329.

[57] A. Shibata, Y. Madi, K. Okada, N. Tsuji, J. Besson, Mechanical and microstructural analysis on hydrogen-related fracture in a martensitic steel, Int. J. Hydro. Energy 44 (2019) 29034–29046.

[58] ASTM E399-09 Standard Test Method for Linear-Elastic Plane-Strain Fracture Toughness K_{IC} of Metallic Materials, 2009.

[59] G. Miyamoto, N. Iwata, N. Takayama, T. Furuhara, Mapping the parent austenite orientation reconstructed from the orientation of martensite by EBSD and its application to ausformed martensite, Acta Mater. 58 (2010) 6393–6403.

[60] T.L. Anderson. Fracture Mechanics, fourth ed., CRC Press, New York, 2017.

[61] K. Okada, A. Shibata, W. Gong, N. Tsuji, Effect of hydrogen on evolution of deformation microstructure in low-carbon steel with ferrite microstructure, Acta Mater. 225 (2022) 117549.

[62] T. Taoka, S. Takeuchi, E. Furubayashi, Slip systems and their critical shear stress in 3% silicon iron, J. Phys. Soc. Jpn 19 (1964) 701–711.

[63] B. Sestak, N. Zarubova, V. Sladek, Slip planes in Fe–3% Si single crystals deformed at 77 K, Can. J. Phys. 45 (1967) 1031–1040.

[64] E. Furubayashi, Behavior of dislocations in Fe-3% Si under stress, J. Phys. Soc. Jpn 27 (1969) 130–146.

[65] L.P. Kubin, F. Louchet, Analysis of softening in the Fe-C system from in situ and conventional experiments - I. In situ experiments, Acta Met. 27 (1979) 337–342.

[66] J.W. Christian, Some surprising features of the plastic deformation of body-centered cubic metals and alloys, Metall. Trans. A 14A (1983) 1237–1256.

[67] L. Huang, D. Chen, D. Xie, S. Li, Y. Zhang, T. Zhu, D. Raabe, E. Ma, J. Li, Z. Shan, Quantitative tests revealing hydrogen-enhanced dislocation motion in α-iron, Nat. Mater. 22 (2023) 710–716.

[68] R. Matsumoto, S.T. Oyinbo, M. Vijendran, S. Taketomi, Hydrogen effect on the mobility of edge dislocation in α-iron: a long-timescale molecular dynamics simulation, ISIJ Int 62 (2022) 2402–2409.

[69] R. Matsumoto, M. Riku, S. Taketomi, N. Miyazaki, Hydrogen–grain boundary interaction in Fe, Fe–C, and Fe–N systems, Prog. Nucl. Sci. Technol. 2 (2011) 9–15.

[70] Y. Momotani, A. Shibata, N. Tsuji, Hydrogen embrittlement behaviors at different deformation temperatures in as-quenched low-carbon martensitic steel, Int. J. Hydro. Energy 47 (2022) 3131–3140.

[71] R. Matsumoto, N. Nishiguchi, S. Taketomi, N. Miyazaki, First-principles calculations of hydrogen effects on the formation and diffusion of vacancies in alpha iron: discussion of the hydrogen-enhanced strain-induced vacancy mechanism, Zairyo 63 (2014) 182–187.

[72] Y. Momotani, A. Shibata, D. Terada, N. Tsuji, Effect of strain rate on hydrogen embrittlement in low-carbon martensitic steel, Int. J. Hydro. Energy 42 (2017) 3371–3379.

[73] Y. Momotani, A. Shibata, T. Yonemura, Y. Bai, N. Tsuji, Effect of initial dislocation density on hydrogen accumulation behavior in martensitic steel, Scr. Mater. 178 (2020) 318–323.

[74] S. Morito, H. Yoshida, T. Maki, X. Huang, Effect of block size on the strength of lath martensite in low carbon steels, Mater. Sci. Eng. A 438-440 (2006) 237–240.

[75] A. Shibata, T. Nagoshi, M. Sone, S. Morito, Y. Higo, Evaluation of the block boundary and sub-block boundary strengths of ferrous lath martensite using a micro-bending test, Mater. Sci. Eng. A 527 (2010) 7538–7544.

[76] P. Sofronis, R.M. McMeeking, Numerical analysis of hydrogen transport near a blunting crack tip, J. Mech. Phys. Solids 37 (1989) 317–350.

[77] D.C. Ahn, P. Sofronis, R. Dodds, Modeling of hydrogen-assisted ductile crack propagation in metals and alloys, Int. J. Fract. 145 (2007) 135–157.

[78] X.Y. Cheng, H.X. Zhang, A new perspective on hydrogen diffusion and hydrogen embrittlement in low-alloy high strength steel, Corros. Sci. 174 (2020) 108800.

[79] G. Miyamoto, A. Goto, N. Takayama, T. Furuhara, Three-dimensional atom probe analysis of boron segregation at austenite grain boundary in a low carbon steel - effects of boundary misorientation and quenching temperature, Scr. Mater. 154 (2018) 168–171.